creative commons
COMMONS DEED

저작자표시-비영리-변경금지 2.0 대한민국

이용자는 아래의 조건을 따르는 경우에 한하여 자유롭게

- 이 저작물을 복제, 배포, 전송, 전시, 공연 및 방송할 수 있습니다.

다음과 같은 조건을 따라야 합니다:

저작자표시. 귀하는 원저작자를 표시하여야 합니다.

비영리. 귀하는 이 저작물을 영리 목적으로 이용할 수 없습니다.

변경금지. 귀하는 이 저작물을 개작, 변형 또는 가공할 수 없습니다.

- 귀하는, 이 저작물의 재이용이나 배포의 경우, 이 저작물에 적용된 이용허락조건을 명확하게 나타내어야 합니다.
- 저작권자로부터 별도의 허가를 받으면 이러한 조건들은 적용되지 않습니다.

저작권법에 따른 이용자의 권리는 위의 내용에 의하여 영향을 받지 않습니다.

이것은 이용허락규약(Legal Code)을 이해하기 쉽게 요약한 것입니다.

Disclaimer

dCollection

이학박사 학위논문

Terahertz nanoscopy of semiconductor surface dynamics

테라파 나노스코피를 통한 반도체 표면 동역학 측정

2018년 2월

서울대학교 대학원

물리천문학부 물리학 전공

최 근 창

Terahertz nanoscopy of semiconductor surface dynamics

지도 교수 김 대 식

이 논문을 이학박사 학위논문으로 제출함
2018 년 2 월

서울대학교 대학원
물리천문학부 물리학 전공
최 근 창

최근창의 이학박사 학위논문을 인준함
2018 년 2 월

위 원 장 박 건 식 (인)

부위원장 김 대 식 (인)

위 원 전 헌 수 (인)

위 원 이 탁 희 (인)

위 원 서 민 아 (인)

Abstract

Terahertz nanoscopy of semiconductor surface dynamics

Geunchang Choi

Department of Physics and Astronomy

The Graduate School

Seoul National University

Most semiconductors have surface dynamics radically different from its bulk counterpart due to surface defect, doping level, and symmetry breaking. Due to the technical challenge of direct observation of the surface carrier dynamics, however, experimental studies have been allowed in severely shrunk structures including nanowires, thin films, or quantum wells where the surface-to-volume ratio is very high. Here, we develop a new type of terahertz (THz) nanoscopy system to investigate the surface dynamics of bulk semiconductors, using metallic nano gap accompanying strong THz field confinement. We observed that carrier lifetimes of InP and GaAs dramatically decrease close to the limit of THz time resolution (~1 ps) as the gap size decreases down to nano scale, and that they return to their original values once the nano-antennas are removed. Furthermore, through both experimental results and calculations, we extracted the surface recombination velocities and diffusion coefficients of the semiconductor materials and that values are consistent with the previous works. Our THz nanoscopy system will open up pathways towards direct, and nondestructive measurements of surface dynamics of bulk semiconductors.

Keyword : nanoscopy, optical pump- Terahertz probe, semiconductor surface, carrier dynamics

Student Number **:** 2012-30901

Table of Contents

List of figures

Chapter 1. Introduction

Surface carrier dynamics in semiconductor materials are related to the band structure of the materials,[1] ion-doping,[2] and surface states,[3-7] which can be drastically different from its bulk carrier dynamics. Understandably, such surface carrier dynamics and surface properties are important factors for the performance of semiconductor-based optoelectronic[8,9] and photovoltaic devices.[10] Despite their importance, direct measurements of the extreme surface properties of bulk semiconductor is challenging because the surface signal is hindered by technical difficulties. Those have been limitedly provided in nanosized structures such as nanowires or thin films which have very large surface to volume ratio.[11-13] Even in nanoscale samples, most carrier dynamics still contain both surface and bulk dynamics; more importantly, it is essential to probe surface dynamics of bulk semiconductors without resorting to nanomaterials of the same material. Optical pump-optical probe technique based on femtosecond laser has been conducted in various semiconductor materials for measurements of different carrier relaxation processes such as ultrafast nonequilibrium dynamics,[14,15] carrier−carrier interaction,[16] and carrier-phonon interaction.[17] As a probe beam, terahertz (THz) waves with low photon energy have many advantages such as being nondestructive and being far below the band gap of the targeted semiconductor materials.[18,19] In this thesis, we measured the surface carrier dynamics of semi-insulating (SI)-InP and SI-GaAs in picosecond time scale using the optical pump-THz probe (OPTP) method. By fabricating nanoantenna onto the targeted materials (SI-InP and SI-GaAs), the carrier dynamics at extreme surface can be efficiently examined. The nanoantenna is composed of slot arrays with a few hundred micrometers in length and a nanoscale width. It enables us to sensitively observe the surface only carrier dynamics of bulk semiconductor in OPTP experiment.

Chapter 2. Terahertz time-domain spectroscopy

2.1 THz wave

Terahertz (THz) wave is the electromagnetic wave between the infrared and microwave, and it shares some properties of them. Like infrared, THz wave travels in a line of sight and is non-ionizing. Like microwave, THz wave transmits non-conducting materials, such as paper, clothing, plastic, and ceramics.[20,21] Mainly the THz zone is from 0.1 THz to 3 THz. The wavelength and photon energy of one terahertz is 300 μm and 4.1 meV, respectively (Fig. 2-1). Typical penetration depth of THz wave is less than that of microwave. By using the properties of THz wave such as high transmission of non-conducting materials, water absorption and low photon energy, there are several applications of THz wave; spectroscopy, medical imaging, and sensing. From the viewpoint of spectroscopy, THz wave can be used for material identification. Many substances have spectral features in THz frequency duo to the rotational vibration mode, intermolecular vibration mode, crystal lattice vibration mode, and so on.[22-24] In the field of medical imaging, the reflected THz wave can imaging skin burns and cancers.[25,26] Especially, the low photon energy of THz enables to imaging human skins without harmful affection to the living organisms. For sensing, THz wave can be used for detection inside the package.[27,28]

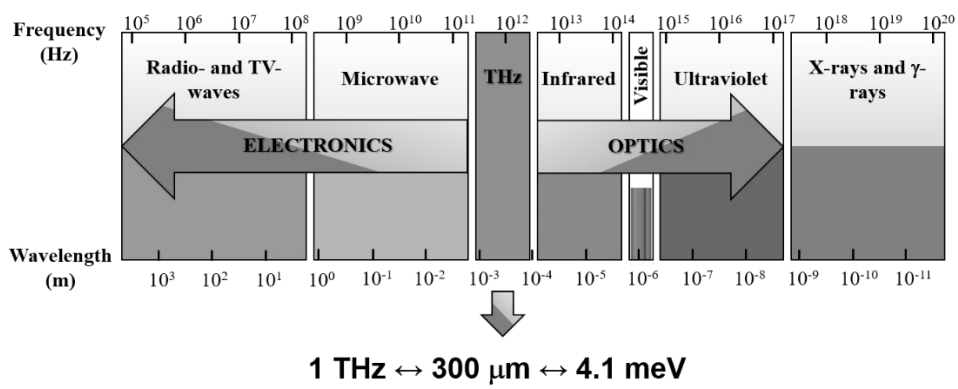

Fig. 2-1 THz wave is the electromagnetic wave between the infrared and microwave.

2.2 THz generation and detection

Typical methods for generating pulsed THz wave are using photoconductive antenna (PCA),[29] optical rectification (OR),[30] and surface-field of semiconductors.[31] Generally, pulse-type THz wave generation is generated by irradiating a femtosecond (10^{-15} s) laser to a semiconductor or optical crystal. In this thesis, we used photoconductive antenna method to generate THz wave.

In the photoconductive antenna method, an antenna electrode is formed of a metal on the low-temperature grown GaAs (LT-GaAs), and a femtosecond laser is irradiated between the electrodes while a voltage is applied across the electrodes (Fig. 2-2). As the electrons and holes excited by the laser beam move to the electrode biased at the semiconductor surface, a fast surge current flows and an electromagnetic wave proportional to the time derivative of the current is radiated from the antenna (Fig. 2-2).[32] This method can obtain comparatively large output compared with other THz pulse generation method and it is easy to change the output by adjusting the laser output and bias voltage.

The electro-optical sampling is a method of measuring the laser beam for detection and the THz wave to be measured simultaneously by irradiating the detection crystal (ZnTe) (Fig. 2-3). The electric field of the THz wave pulse induces birefringence in the crystal by the electro-optic effect. When the laser beam for linearly polarized detection is irradiated to the crystal, the two polarization components in the propagation direction undergo different refractive indices, resulting in a phase delay between the two components. After then, the laser beam in which the phase delay occurs is elliptically polarized through the λ/4 wave plate and divided into two polarized components having different intensities by the prism and is incident on the balanced photodiode. This current value is proportional to the intensity of the electric field of the THz wave.

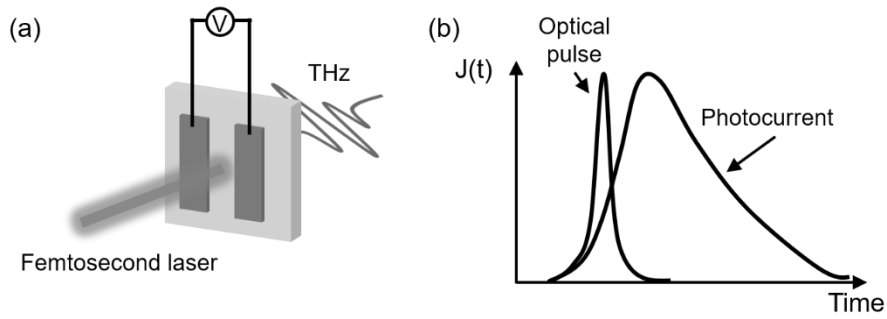

Fig. 2-2 (a) Photoconductive antenna for THz generation. (b) Calculated photocurrent in the photoconductive antenna and amplitude of the radiated field versus time.

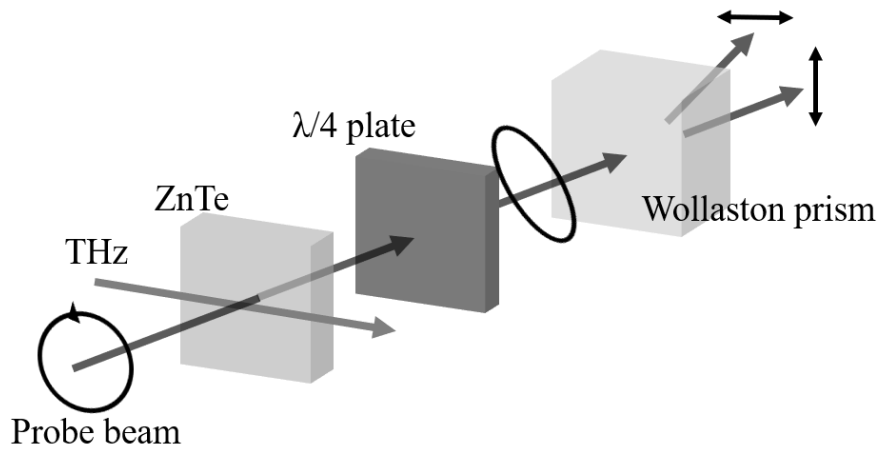

Fig. 2-3 Schematic of electro-optic sampling for THz detection.

2.3 THz time domain spectroscopy

Figure 2-4 is the experimental setup of terahertz-time domain spectroscopy. The laser beam from the femtosecond Ti:sapphire laser (80 MHz repetition rate, 800 nm center wavelength and 130 fs pulse duration) is divided into a generation beam and a detection beam by a beam splitter. The generation beam is irradiated to the photoconductive antenna to generate a THz wave. The generated THz wave is collected by high-resistance silicon lens and guided by off-axis parabolic mirror. The detection beam and THz wave are focused on ZnTe crystal for electro-optic detection. After then, detection beam divided into x- and y-polarized components by Wollaston prism is incident on the balanced photodiode. This current value is proportional to the intensity of the electric field of the THz wave. For sampling the THz pulse, we used time delay line at the THz generation beam. In Fig. 2-5 (a), the measured THz electric field amplitude is plotted in time domain. By considering the phase retardation due to the THz induced birefringence in the ZnTe and THz beam size, the maximum THz electric field was extracted with 30 V/cm at the focus. The frequency spectrum of the THz wave is obtained by Fourier transform of time domain THz pulse (Fig. 2-5 (b)).

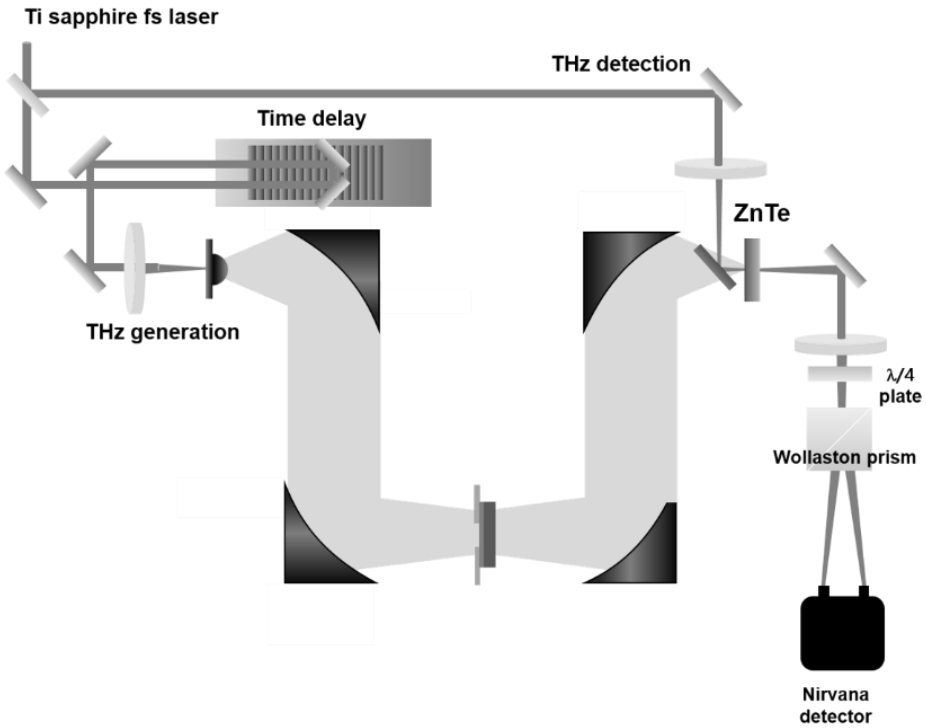

Fig. 2-4 Experimental setup of terahertz time domain spectroscopy. THz wave is generated by photoconductive antenna method and detected by electro-optic sampling of ZnTe crystal.

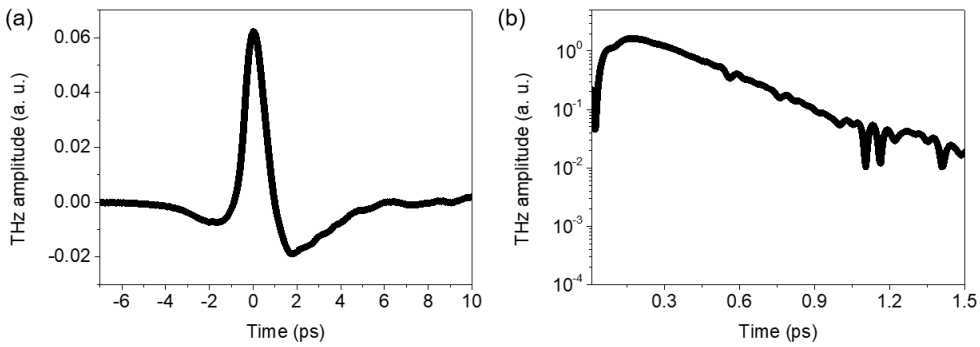

Fig. 2-5 (a) Electro-optic sampling signal of THz electric field emitted from the biased LT-GaAs in the time domain. (b) Fourier transformed spectrum of the signal (a).

Chapter 3. Terahertz nano-slot antenna

3.1 Nanofocusing of THz wave

Growing the interest of nanoscale materials, it is required to focus the THz waves into nanosize. Nanosized focusing of THz wave is conducted by using metallic nanostructures in order to overcome the diffraction limit. When the THz wave is focused in nanosized, not only effectively interact with nanoscale materials but also accompanying large field enhancement of THz wave.[33-36] Such a light confinement at nanoscale can be achieved with metallic nanostructures in a wide range of frequencies, giving many applications using the enhanced field.[37-44] However, since the enhanced field increases as the accumulated charges increase by the electromagnetic wave, the THz wave can have a huge field enhancement.[33] In THz frequency regime, the field confinement into the nanosized volume of its large wavelength increases the field enhancement up to ~ 10^3.[45-47] The large field enhancement of THz wave enables to observe the enhanced absorption and nonlinearities in THz frequency.[48-52]

3.2 THz nano-slot antenna

Among the various metallic nanostructures, a negative patterned nano-slot antenna which is composed of metallic rectangular holes has several advantages. Since the electromagnetic waves are transmitted only through the inside the gap, we can detect background free signals and it is easy to define exact field enhanced volume (Fig. 3-1). The nano-slot antenna has resonant frequency which is determined by length of antenna, refractive index and thickness of substrate.[53-55] Generally, the THz nano-slot antenna is composed metallic hole array with few hundred micrometer length and nanometer width.

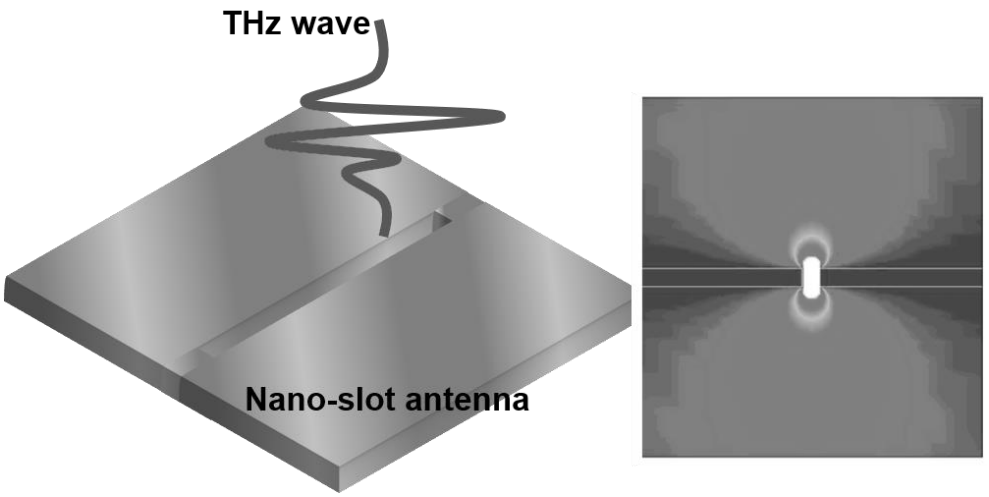

Fig. 3-1 Schematic of THz nano-slot antenna and THz field distribution around the antenna.

3.3 Nano-slot antenna fabrication

THz nano-slot antenna can be fabricated by various methods, such as electron beam lithography, focused ion beam, atomic layer lithography, and so on. In order to effectively fabricate few hundreds width slot antenna, electron beam lithography is widely used, because the focused ion beam is time consuming and atomic layer lithography is optimized for sub-10 nm width antenna. Figure 3-2 shows electron beam lithography fabrication process. First, negative electron beam resist is spin-coated on target substrate and baked. Then, the desired pattern of the resist is exposed by scanning electron beam. After removing the unexposed area by development process, metal film with adhesive layers are deposited on the sample. Finally, nano-slot antenna is made after lift-off process. Figure 3-3 is scanning electron microscopy image one of the electron beam lithography sample. In order to increase signal-to-noise ratio, the nano-slot antennas are made of arrays with an x-direction separation of 50 μm and a y-direction separation of 10 μm.

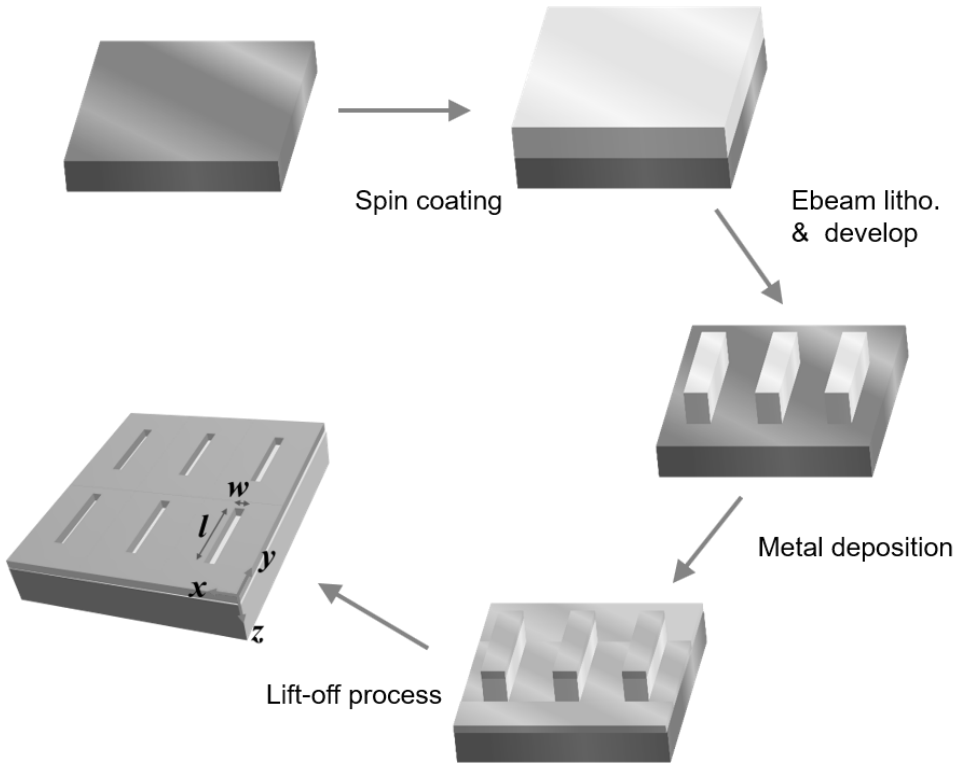

Fig. 3-2 Schematic of electron beam lithography process (spin coating – patterning – develop – metal deposition – lift off).

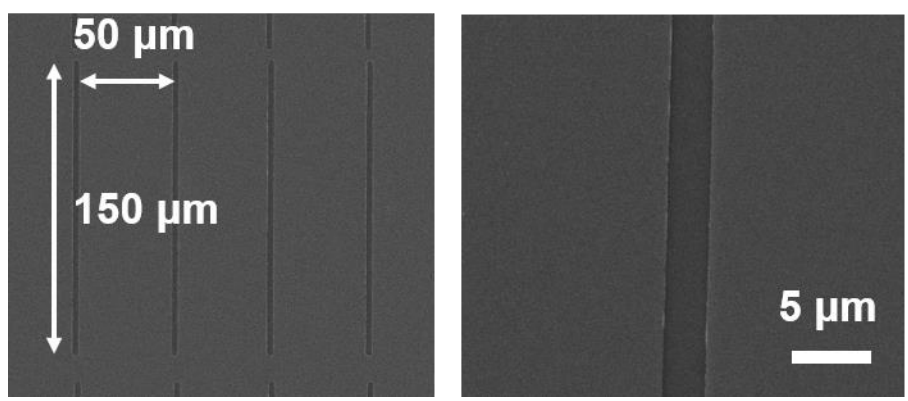

Fig. 3-3 Scanning electron microscopy image of electron beam lithography sample. The length of antenna is 150 μm with 2 μm width.

3.4 Transmission of nano-slot antenna

Most of the THz experiment is conducted by the THz transmission of antennas. When a nano-slot antenna is placed on the THz focusing spot, normalized transmitted amplitude t was used for characterizing samples. For the nano-slot antenna transmission, THz polarization was perpendicular to the long axis of the slot. The normalized transmitted amplitude $t(\omega)$ is shown as follows,

$$t(\omega)=\frac{\left|E_{\text{sample}}(\omega)\right|}{\left|E_{\text{ref}}(\omega)\right|},$$

where $E_{\text{sample}}(\omega)$ and $E_{\text{ref}}(\omega)$ are the transmitted electric field amplitude for the samples and the bare substrate. We plot frequency dependent transmission data for the different nano-slot antenna samples on GaAs substrate (Fig. 3-4). Compared to the broad THz wavelength source (Fig. 3-4 (a)), the nano-slot antennas have narrow resonant frequency (Fig. 3-4 (b), (c), (d)).

The transmitted far field amplitude is related to the enhanced near field amplitude at the gap through Kirchhoff integral formalism.[56]

When an observation point of the transmitted field is located far from the slot hole, the electric field can be approximated by the Kirchhoff integral,

$$\vec{E}(\vec{r})=\frac{ie^{i\vec{k}\cdot\vec{r}}}{2\pi r}\vec{k}\times\int_A\hat{n}\times\vec{E}(\vec{r}')e^{-i\vec{k}\cdot\vec{r}'}da',$$

where $\vec{r}'$ is the coordinate of the element of the surface area of the hole, A, is the distance from origin, O, to the observation point, $\hat{n}$ is the surface normal, and $\vec{k}$ is the wave vector in the direction of the observation point. For an incident wave polarized in the horizontal direction and impinging upon the hole at the normal incidence, we can use the scalar expression and define the diffracted horizontal component of electric fields

$$E^{far}=\frac{e^{ikr}}{i\lambda r}\int_A E^{near}(r')da'=\frac{e^{ikr}}{i\lambda r}\left\langle E^{near}\right\rangle A,$$

where the bracket means the averaged near field over the hole area, i.e.

$$\left\langle E^{near} \right\rangle = \frac{1}{A}\int_A E^{near}(r')da'.$$

According to this formalism, the transmitted far field through the hole is proportional to the near field distribution inside the hole. Therefore, the near field enhancement can be estimated from the far field measurement, corresponding to $t(\omega)/\beta$, where β is the hole-to-aperture area ratio.

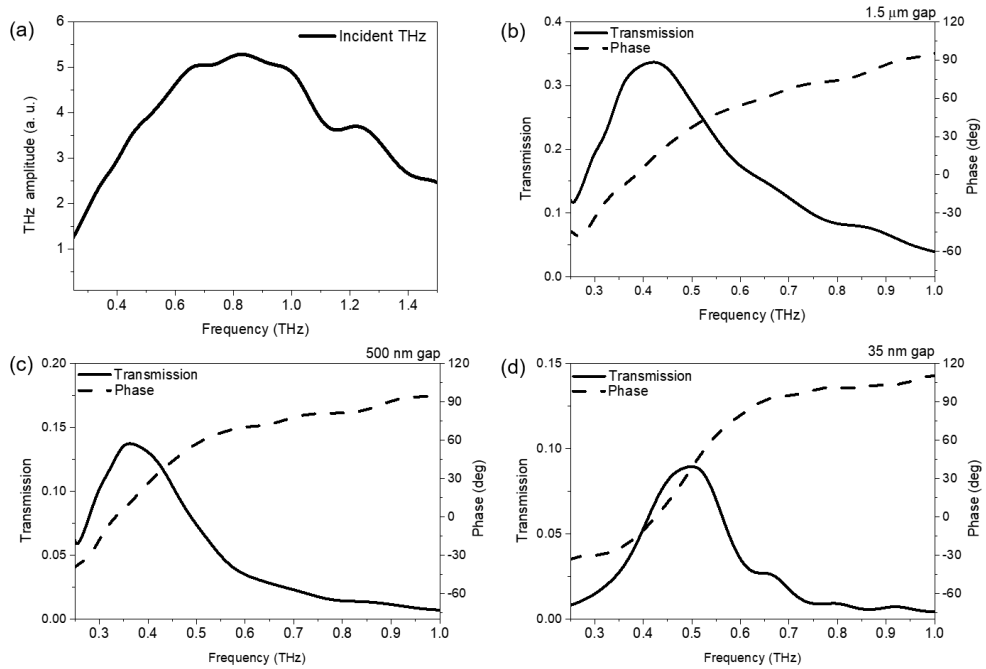

Fig. 3-4 (a) Fourier-transformed spectra of incident THz wave. THz transmission and phase of (b) 1.5 μm gap, (c) 500 nm gap, and (d) 35 nm gap antennas.

Chapter 4. Semiconductor surface carrier dynamics

4.1 Semiconductor surface

Semiconductor materials usually have different carrier dynamics dependent on band structure,[1] doping,[2] and surface state.[3-7] At the semiconductor surface, the Fermi-level is pinned due to the surface trap energy, leading to band bending upward and to higher Schottky barrier height (Fig. 4-1). This Schottky barrier height results in the short carrier recombination time of the semiconductors. Carriers at the surface have not only short carrier lifetime, but also small signal because of the its small volume. Compare to the surface carrier dynamics, bulk carrier dynamics has relatively long time and large signal. In general carrier dynamics of semiconductor materials, these two surface and bulk carrier dynamics are combined, and the surface carrier dynamics is hidden by the bulk carrier dynamics (Fig. 4-2). However, direct measurements of the surface properties have been hindered by technical difficulties, and eventually the surface carrier dynamics is not dominantly observed. Despite of the technical difficulties to observing surface of semiconductor, such surface carrier dynamics and surface properties are important for the performance of semiconductor-based optoelectronic[8,9] and photovoltaic devices.[10]

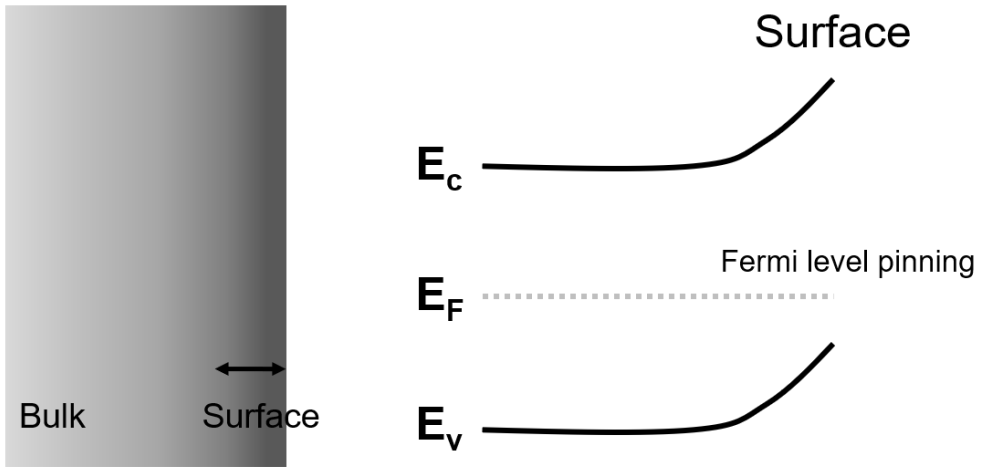

Fig. 4-1 Schematic of semiconductor. At the semiconductor surface, the Schottky barrier is occurred by the Fermi-level pinning, resulting short carrier lifetime.

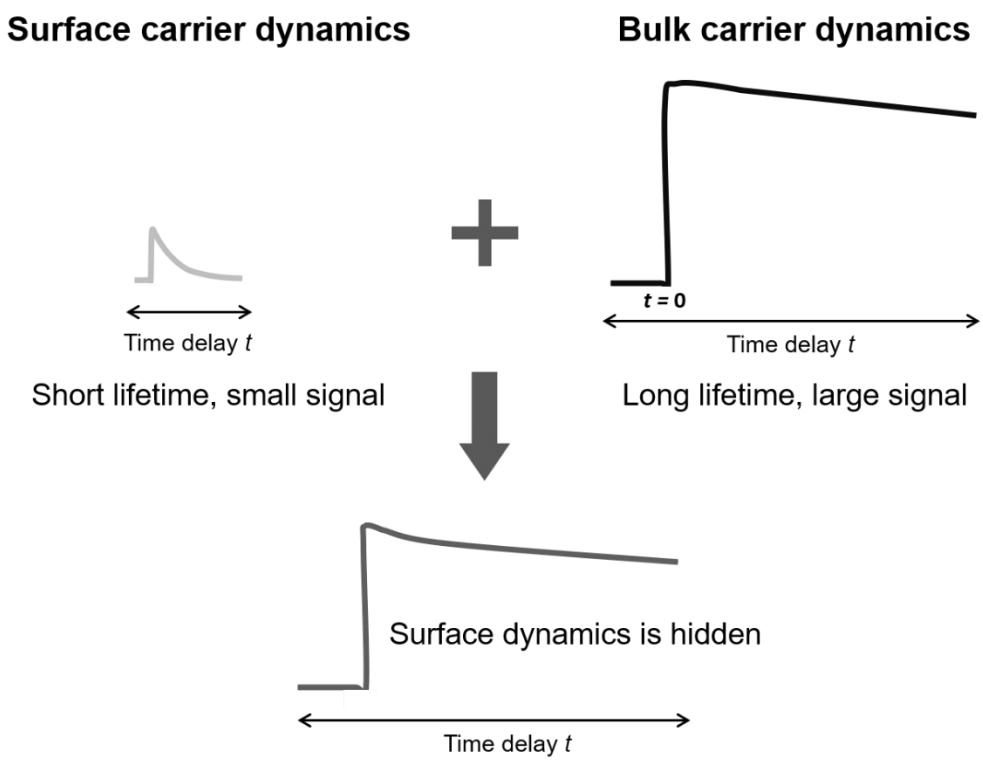

Fig. 4-2 Carrier dynamics from the semiconductor surface and bulk.

4.2 Observation of semiconductor surface dynamics

In order to observe the carrier dynamics of the semiconductors, femtosecond pump-probe method is used. As shown in Fig. 4-3, pump beam excites carriers and the reflection of probe beam is changed by the number of excited carriers. In the pump-probe experiment, since the carrier excitation depth from the semiconductors surface is determined by pump penetration depth, carrier dynamics of bulk semiconductor contains both surface and bulk dynamics. When we decrease the penetration depth of pump beam by changing pump wavelength, the bulk effect is reduced, and surface carrier dynamics can be observed. Therefore, to observe the surface carrier dynamics of bulk semiconductor, the use of a short wavelength pump or probe beam is necessary for generating small pump depth or observing small probe depth. However, the use of a high energy pump for small pump depth result in intervalley scattering carrier dynamics.[57-59] Changing probe wavelength also can affect the carrier dynamics.[4,60]

Another method for measuring surface carrier dynamics is the usage of nanosized semiconductor materials. It is possible to measure the surface carrier dynamics of the semiconductor without changing the wavelength of the pump and probe beam. By fabricating a nanosized semiconductor having a large surface-to-volume ratio of the material itself such as a nanowire or a nanosized sample, we can measure surface carrier dynamics (Fig. 4-4).[11-13] Because the surface carrier dynamics is hidden by bulk carrier dynamics, reduction of sample size leads to increasing surface signal. In this case, the semiconductor itself is permanently deformed and cannot be returned to the original bulk semiconductor. Even in nanoscale samples, most carrier dynamics still contain both surface and bulk dynamics. More importantly, it is essential to probe surface dynamics of bulk semiconductors without resorting to nanomaterials of the same material.

In the next chapter, we reduce the bulk effect of the semiconductor by using the field confinement of THz nano-slot antenna. This THz nano-slot antenna enables to observe semiconductor surface carrier dynamics without any destruction of bulk semiconductor and change of pump/probe wavelength.

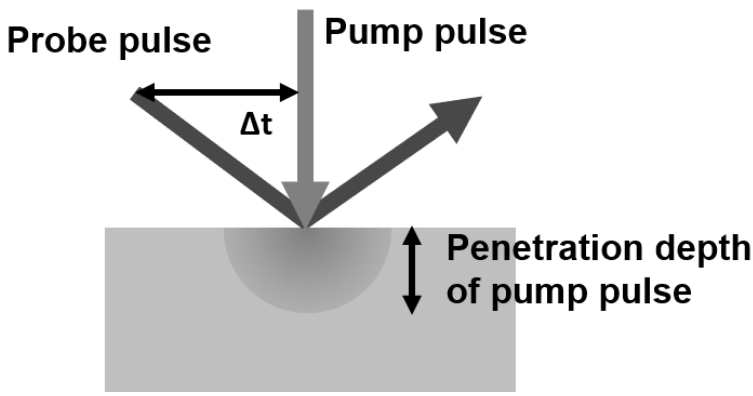

Fig. 4-3 Schematic of femtosecond pump-probe method. Penetration depth of pump pulse determines the carrier excitation depth from semiconductor surface.

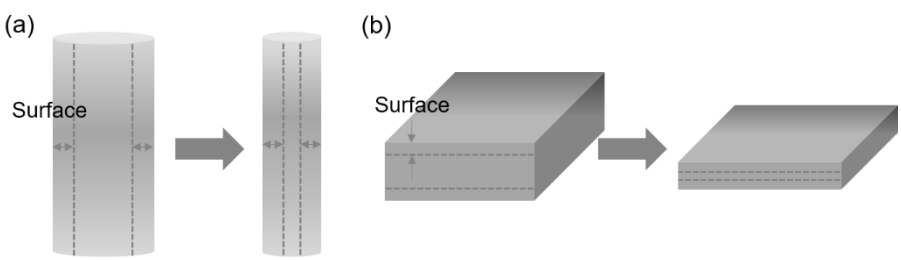

Fig. 4-4 Increase of surface-to-volume ratio of semiconductor. By reducing of semiconductor size such as (a) diameter of nanowire and (b) thickness of semiconductor film, surface-to-volume ratio of the semiconductor can be increased.

4.3 Target semiconductor materials (InP and GaAs)

Semiconductor materials have electrical conductivity values between that of a conductor and an insulator. The band gap of semiconductors are one of two types, a direct band gap or indirect band gap. If the crystal momentums of minimal energy state in the conduction band and maximal energy state in the valence band are the same, it is called a direct band gap. Otherwise, it is called an indirect band gap. In this thesis, direct band gap semiconductors (InP and GaAs) are used as a target semiconductor for comparing surface carrier dynamics.

As an III-V direct-gap semiconductor, InP and GaAs have similar bandgap energy (InP; 1.344 eV, GaAs; 1.424 eV). However, several electronic properties of these two semiconductors are different such as surface recombination velocity and free-carrier saturation limits.[61] Especially, the intrinsic InP and GaAs have remarkable difference in surface recombination velocity. Since the energy of surface states due to dangling bonds in InP is close to the conduction band while that of surface states in GaAs is closer to the mid gap, the Fermi-level at the surface of GaAs is pinned near the mid gap leading to band bending upward and to higher Schottky barrier height. This Schottky barrier height results in the surface recombination velocity of GaAs being faster than that of InP even though they have similar band structures and optical properties. General surface recombination velocity of intrinsic InP and GaAs is ~ 10^2 cm/s and ~ 10^6 cm/s, respectively.[62,63] However, such surface recombination velocity changes dependent on ion doping, surface passivation. For example, semi-insulating (Fe-doped) InP for high resistivity shows the surface recombination velocity ~ 10^5 cm/s[64] and surface passivated GaAs is reduced the surface recombination velocity to ~ 10^3 cm/s.[65] For experiment, we used semi-insulating (SI)-InP and SI-GaAs

that have high resistivity for the THz transmission.

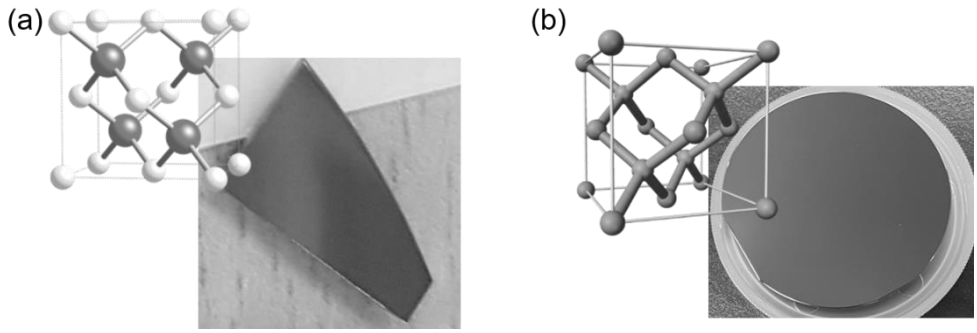

Fig. 4-5 Target semiconductor materials. (a) InP and (b) GaAs have similar properties such as crystal structure (Zinc Blende) and band gap energy (InP = 1.344 eV, GaAs = 1.424 eV).

Chapter 5. Terahertz nanoscopy of bulk semiconductor surface dynamics

5.1 Terahertz nanoscopy for semiconductor surface dynamics

To observe the semiconductor surface dynamics, it has to change the wavelength of the pump/probe beam or fabricate small size semiconductor materials to minimizing the bulk effects. However, in this thesis, THz nanoscopy antenna is used for reducing bulk effect of semiconductor materials. The THz nanoscopy antenna is composed of slot antennas array with a few hundred micrometers in length but with a nanoscale width, accompanying strong field confinement.[33] It enables us to sensitively capture the surface only carrier dynamics of bulk semiconductor in OPTP experiment. This THz nanoscopy antenna method requires antenna fabrication onto the semiconductor substrate, but we don't need to change pump/probe wavelength and change semiconductor size.

The THz nanoscopy antennas were fabricated by electron beam lithography, and we used focused ion beam for 50 nm gap sample or atomic layer lithography for 35 nm gap sample. The slot antennas with gap size from 3 μm to 150 nm gap were fabricated by electron beam lithography. To avoid direct metal contact on substrates, 10 nm-thick Al_2O_3 (aluminum oxide layer) and 50 nm-thick gold are subsequently deposited on InP and GaAs substrates by electron beam evaporator. We used focused ion beam for 50 nm-gap-patterned InP sample. The gold film and InP are separated by 2 nm-thick aluminum oxide layers. All slot antennas have the same length of 150 μm and the same period of 50 μm. For 35 nm-gap sample of GaAs, 50 μm × 50 μm square ring antennas were fabricated by atomic layer lithography[47] and subsequently milling process is conducted to increase the transmission signal.[66] All of the samples have a resonance frequency at 0.4 ~ 0.5 THz as shown in Fig. 3-4.

In order to observe the surface carrier dynamics of bulk semiconductor, we used field confinement of nano-slot antenna as well as field enhancement.

As shown in Fig. 5-1, the THz field intensity ($|E_x|^2$) near the nano-slot antenna confined to the surface of substrate, which represents that small surface volume is detected. However, if the field enhancement of the nano-antenna is ignored, the surface dynamics is hardly detectable due to the small volume. Therefore, in the THz nanoscopy method, both of field confinement and enhancement are important factor to observe the surface carrier dynamics.

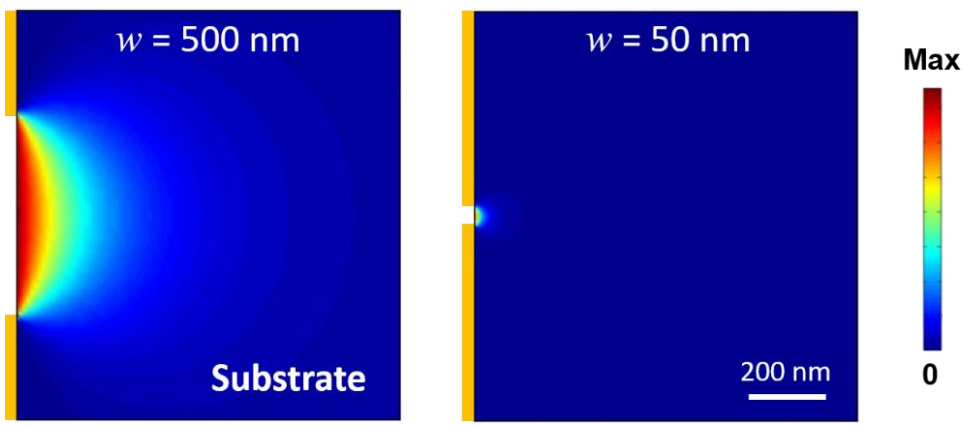

Fig. 5-1 Electric field intensity $|E_x|^2$ distribution of THz probe beam near 500 nm and 50 nm sized nano-slot antenna on InP substrate, obtained by analytical calculation based on modal expansion. Strong confinement of the THz field to the surface enables to observe surface carrier dynamics.

5.2 Optical pump-THz probe

Femtosecond pump-probe technique is used to measure excited carrier dynamics or absorption of samples in the excited state. Using optical pump-optical probe technique, there has been conducted in various semiconductor materials for measurements of different carrier relaxation processes. As a probe beam, THz waves with low photon energy have many advantages such as being nondestructive and being far below the band gap of the semiconductor materials.[67,68] Furthermore, the THz wave enables to utilize large field confinement and enhancement of nano-slot antenna.

For the optical pump THz probe (OPTP) experiment, a femtosecond Ti:sapphire laser is divided into three paths, one is for optical pump and the others are for THz time domain spectroscopy (in Fig. 5-2). The optical pump is focused on a sample located at the focal spot of THz waves with various power. The optical pump beam impinges on a sample at an angle of 45° while the THz probe beam is normally incident. Time delay line is added at the optical pump line in order to delaying time of pump and probe.

Because THz waves are sensitive to conductivities of the sample materials, the optical pump response of semiconductors can be described with interband conductivities which depend on photoexcited carrier densities. We monitored change in THz transmission, $\Delta T/T$ ($= (T-T_{pump})/T$), at the peak of THz signal in time domain by changing relative time delay of the optical pump beam. Figure 5-3 shows that how the carrier dynamics of semiconductor is observed by OPTP. Pump beam at 800 nm wavelength excites a sample with femtosecond time scale before THz probe beam is pulsed on the sample. After short time delay, the THz probe beam proportionally decrease as the number of excited carriers. By monitoring the THz change as a function of delay time, we can obtain the carrier dynamics.

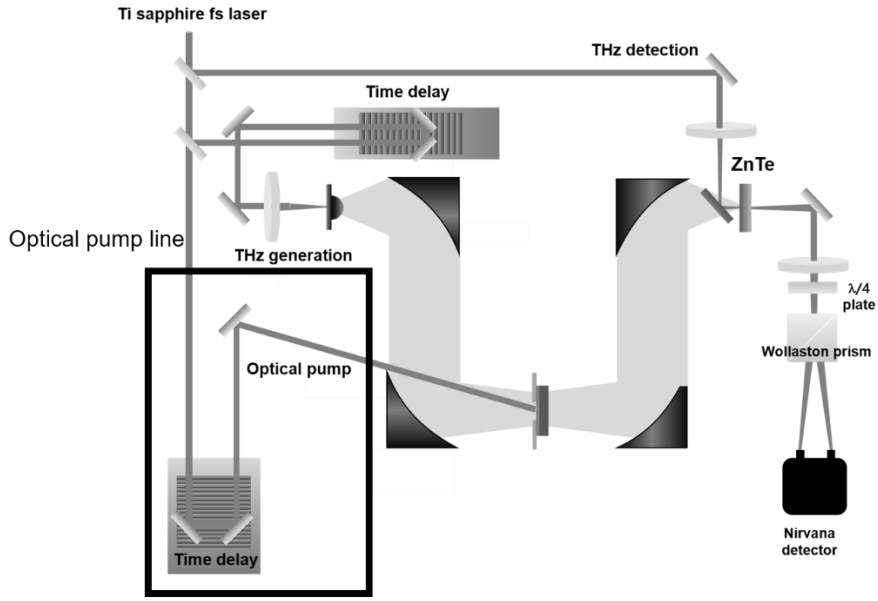

Fig. 5-2 Optical pump-THz probe spectroscopy setup. From the time domain THz spectroscopy setup, optical pump beam is added with time delay line.

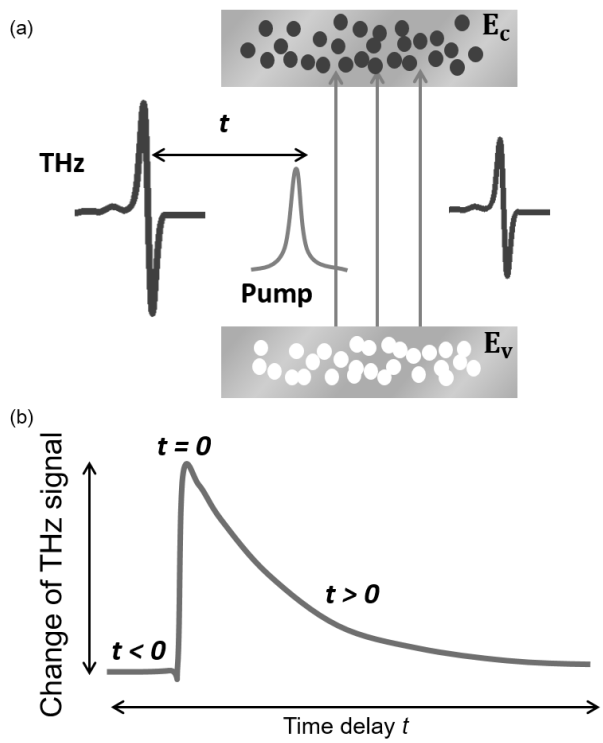

Fig. 5-3 (a) Schematic of optical pump-THz probe measurement. The optical

pump excites carriers balance band to conduction band. Then time delayed THz probe is absorbed by the number of excited carriers. (b) Optical pump-THz probe signal as the pump-probe time delay.

5.3 Experimental results

In experiment, we used OPTP method for measuring semiconductor carrier dynamics. Before using nanoscopy method, we first considered the metal-semiconductor contact effect. Direct metallic nano-slot antenna fabrication on the semiconductor substrate can affect semiconductor surface carrier dynamics due to the metal-semiconductor contact, which changes surface states of semiconductors and carrier dynamics. We measured the carrier dynamics of InP and GaAs with Cr/Au deposition. As a result, compared to the original bare substrate, the carrier dynamics of InP with metal contact is radically changed, representing that the semiconductor surface state is changed (Fig. 5-4). However, the carrier dynamics of GaAs shows same carrier dynamics after contacting the metal. To avoid the direct metal contacts on target semiconductors, we added aluminum oxide layers between the semiconductors and gold nano-slot antenna. As shown in Fig. 5-5 (a) which is a cross sectional view, the nano-slot antenna is spaced by aluminum oxide layer and surface probe regime of the nano-slot antenna is not covered by any oxide or metal layer. We measured carrier dynamics of semiconductors with different aluminum spacing layers from 2 nm to 10 nm (Fig. 5-5 (b-e)). Figure 5-6 (a) and (b) represent the carrier dynamics of different aluminum oxide spacing samples for InP and GaAs substrate. Avoiding direct metal contact, 2 nm thick aluminum oxide layer effectively passivates the semiconductor surface. For the nano-slot antenna experiment, we added 10 nm aluminum oxide layer for the samples fabricated by electron beam lithography and 2 nm aluminum oxide layer for the other samples.

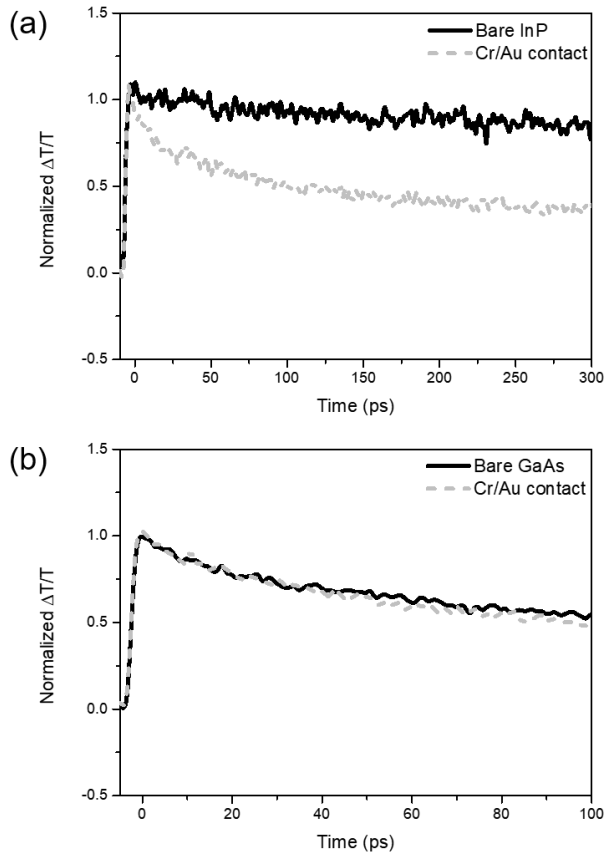

Fig. 5-4 Normalized THz transmission changes of bare substrate and Cr contacted substrate for (a) InP and (b) GaAs. The carrier dynamics of InP with metal contact is radically changed, while that of GaAs with metal contact shows same carrier dynamics of original bare substrate.

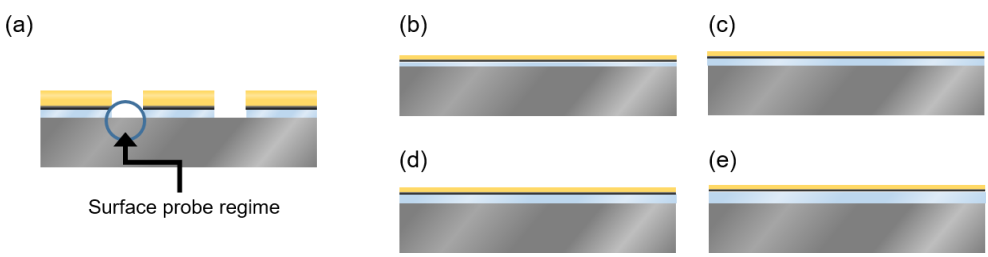

Fig. 5-5 (a) Schematic of cross sectional view of nano-slot antenna, showing that the surface probe regime is not covered any oxide or metal. (b-e) side view of aluminum oxide spaced metal films on semiconductor substrate. Between the Cr/Au and semiconductor, aluminum oxide layer is (b) 2 nm, (c)

4 nm, (d) 6 nm, and (e) 10 nm.

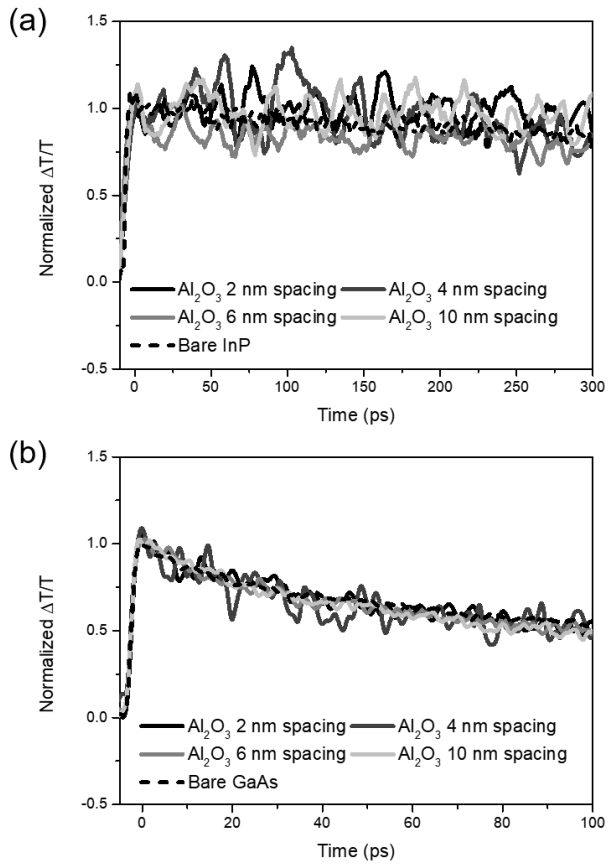

Fig. 5-6 Normalized THz transmission changes for (a) GaAs and (b) InP with different aluminum oxide layer thickness of Fig. 5-5 (b-e).

Figure 5-7 and 5-8 show normalized transmission changes of THz probe beam as a function of the OPTP time delay for bare and nano-slot antenna patterned InP and GaAs at various gap sizes. First, we measured the carrier dynamics of bare InP and nano-slot antenna samples. As a result, compared to the very long carrier lifetime of bare InP up to several hundreds of picoseconds, we can observe short carrier lifetimes as the width of antenna decreases (Fig. 5-7 (a)). When we decrease the gap size down to nanoscale. τ dramatically decreases to picosecond scale ($\tau_{InP} \sim 2.1$ ps for 50 nm gap). Compare to the bare carrier lifetime, this indicates that we have found hidden

carrier lifetime that we could not predict. Figure 5-7 (b) is the intensity distribution of THz near field near the antenna. The results represent that hidden surface carrier dynamics can be observed by strong field confinement of nano-slot antenna. For GaAs samples, we can observe the same tendency and shorter carrier lifetimes (Fig. 5-8). For bare GaAs and nano-slot antenna samples, carrier lifetime decrease as the gap size decreases and the carrier lifetime is saturated at 2 ps close to the limit of THz time resolution limit in the inset of the Fig. 5-8 (τ_{GaAs} ~ 2 ps for 200 nm gap and for 35 nm gap). The faster carrier lifetimes in nano-slot antenna samples originate from the extreme surface, observed by our THz nanoscopy system. As we mentioned in chapter 4, the Fermi-level pinning position which is related to the dangling bonds energy results in the surface recombination velocity of GaAs being faster than that of InP even though they have similar band structures and optical properties. As a result, we could observe that the carrier lifetime of GaAs is shorter than that of InP for the same gap size antenna.

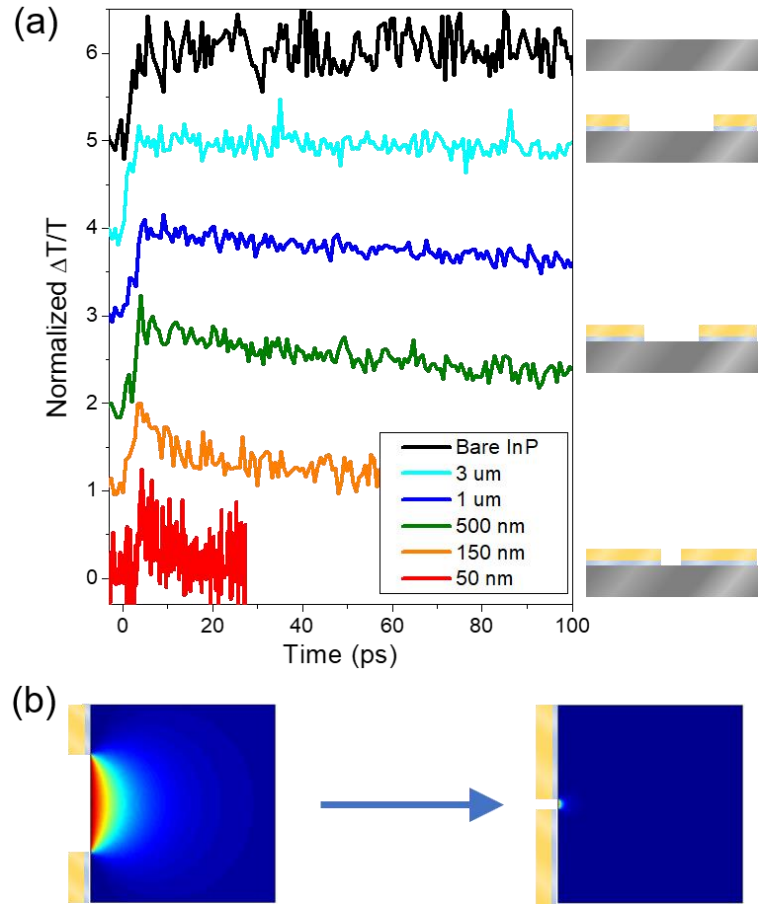

Fig. 5-7 (a) Normalized THz transmission changes for different metallic gap samples on InP and as a function of pump−probe delay time. The decaying time constants τ of InP are 73, 28, 5, and 2.1 ps for the gap sizes of 1 μm, 500 nm, 150 nm, and 50 nm, respectively. (b) Electric field intensity $|E_x|^2$ distribution of THz probe beam near the nano-slot antenna on InP substrate. Strong confinement of the THz field to the surface enables to observe surface carrier dynamics, resulting that hidden surface carrier dynamics is observed.

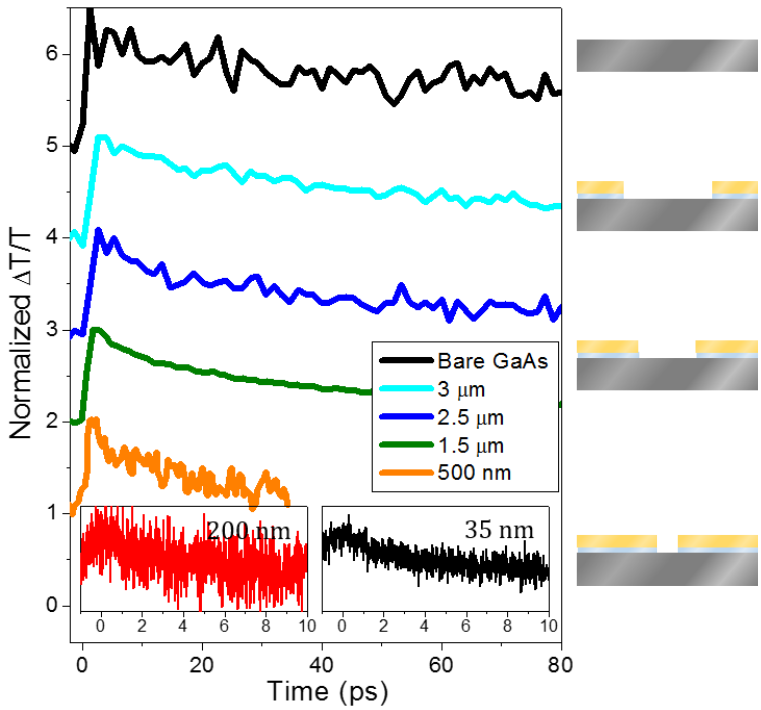

Fig. 5-8 Normalized THz transmission changes for different metallic gap samples on GaAs as a function of pump−probe delay time. The decaying time constants τ of GaAs are 86, 35, 22, 18, and 7.5 ps for bare GaAs and the gap sizes of 3 μm, 2.5 μm, 1.5 μm, and 500 nm, respectively. Further narrow gap (200 and 35 nm) of GaAs, the carrier lifetimes are saturated due to the THz time resolution limit.

Carrier dynamics after removing the nano-slot antenna patterns is measured because the nanoscopy method enables permanent reuse of target materials. We used 150 and 500 nm width nano-slot antenna for InP and GaAs, respectively, and removed the nano-slot antenna by using hydrogen fluoride (HF) solution which etches the aluminum oxide layer with gold nano-slot antenna. As shown in Fig. 5-9, the bulk lifetimes of semiconductors (InP and GaAs) are completely restored after removing the nano-slot antenna patterns. To measure the surface carrier dynamics effectively, it has been required to severely change surface-to-volume ratio by newly fabricating nanowires or nanomaterials[11-14,69] otherwise to use shorter wavelength as a probe beam for much smaller penetration depth.[70] However, by adopting the nanoscopy method, we can control the THz probe depth at fixed frequency and measure carrier dynamics without any destruction of bulk semiconductors.

Moreover, we can choose a broad range of wavelengths for carrier dynamics measurement, changing the antenna length. As the frequency of probe beam can be tuned by changing the length of the antenna, we fabricated 0.45 THz, 1 THz, and 1.3 THz resonant frequency antennas (150 μm, 60 μm, and 40 μm length, respectively) with a 2 μm width on the GaAs substrate (Fig. 5-10 (a)). THz transmission for the antennas increases as the resonant frequency is close to lower. This is due to the large field enhancement for the longer wavelength, though the antennas have same width. In the OPTP experiment, carrier dynamics of the nano-slot antennas are independent of their resonant frequencies and field enhancement (Fig. 5-10 (b)). To compare width dependence, we fabricated same length of antennas with a 400 nm width on GaAs substrate (Fig. 5-11). THz transmission increases due to the field enhancement and the carrier dynamics are independent on the resonant frequency, same as in Fig. 5-10 (a), while the fast carrier dynamics are observed in the 400 nm width antennas for the strong field confinement (Fig. 5-11 (b)). Because the surface carrier dynamics is obtained by field

confinement near the gap, broad range of wavelength can be selected as a probe beam as long as the antenna width is smaller than the wavelength. As an example, for 500 nm gap, analytical calculations show that the wavelength from 0.1 THz to 10 THz has almost same confined depth (Fig. 5-12), presenting the possibility that probe wavelengths can be extended to the infrared range. However, there are some limits to probe surface carrier dynamics: the signal-to-noise ratio decreases due to the small confined probe volume and the target material has to be detectable in transmission geometry.

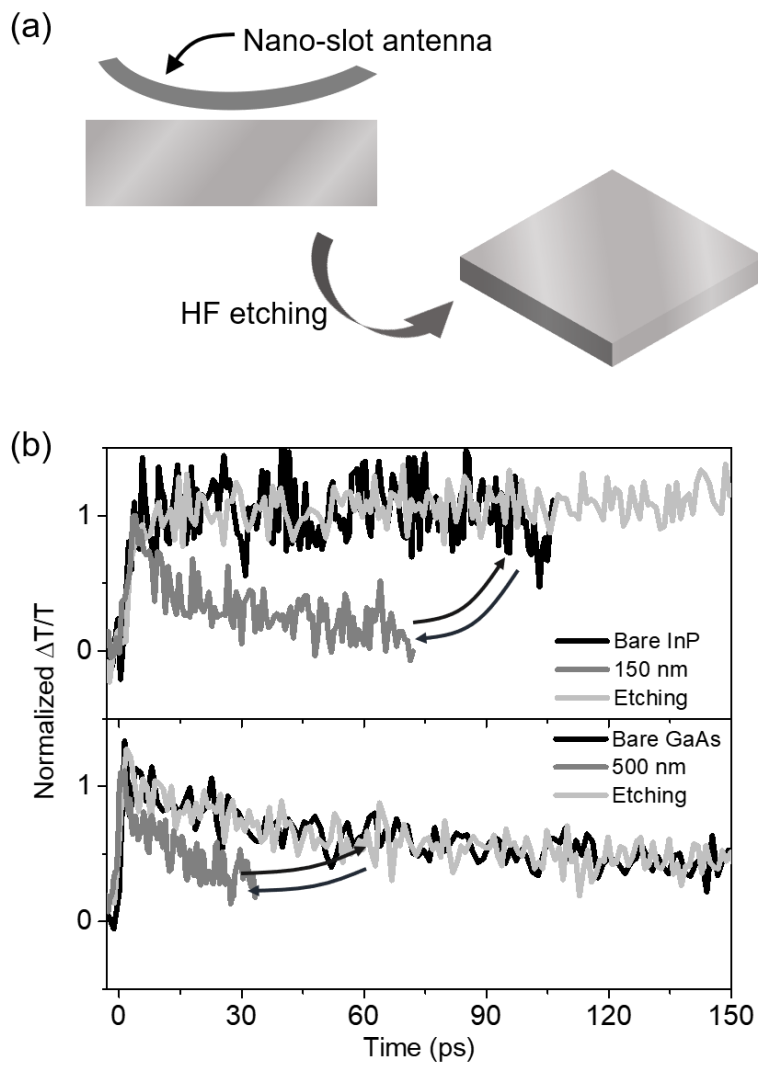

Fig. 5-9 Carrier dynamics of bare and nano-slot antenna on InP (top) and

GaAs (bottom) measured from optical pump THz-probe spectroscopy. The gap size is 150 and 500 nm for InP and GaAs, respectively. Once the nano-slot antennas are etched, the carrier recombination processes are completely recovered to the characteristics of bare samples.

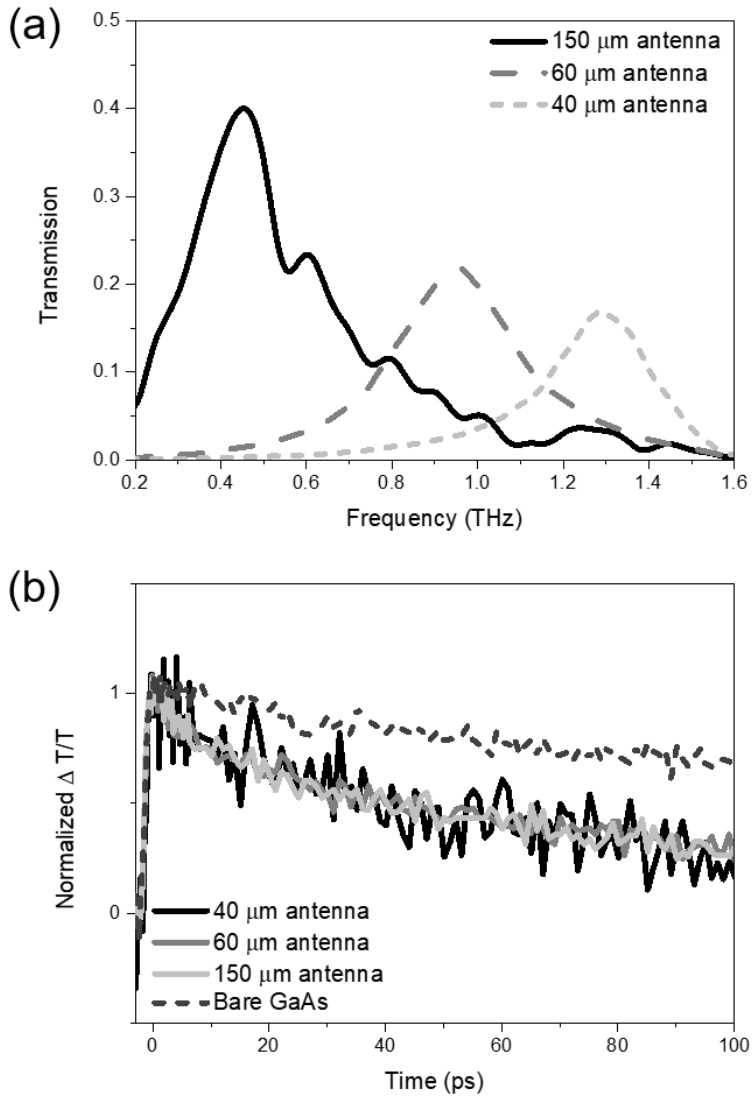

Fig. 5-10 (a) THz transmission for 150 μm length, 60 μm length, and 40 μm length antennas on GaAs substrate. The width of the antennas is fixed at 2 μm. THz transmission increases for the longer length of antenna due to the larger field enhancement. (b) Normalized THz transmission changes for different length antenna samples. The optical pump power is 200 mW.

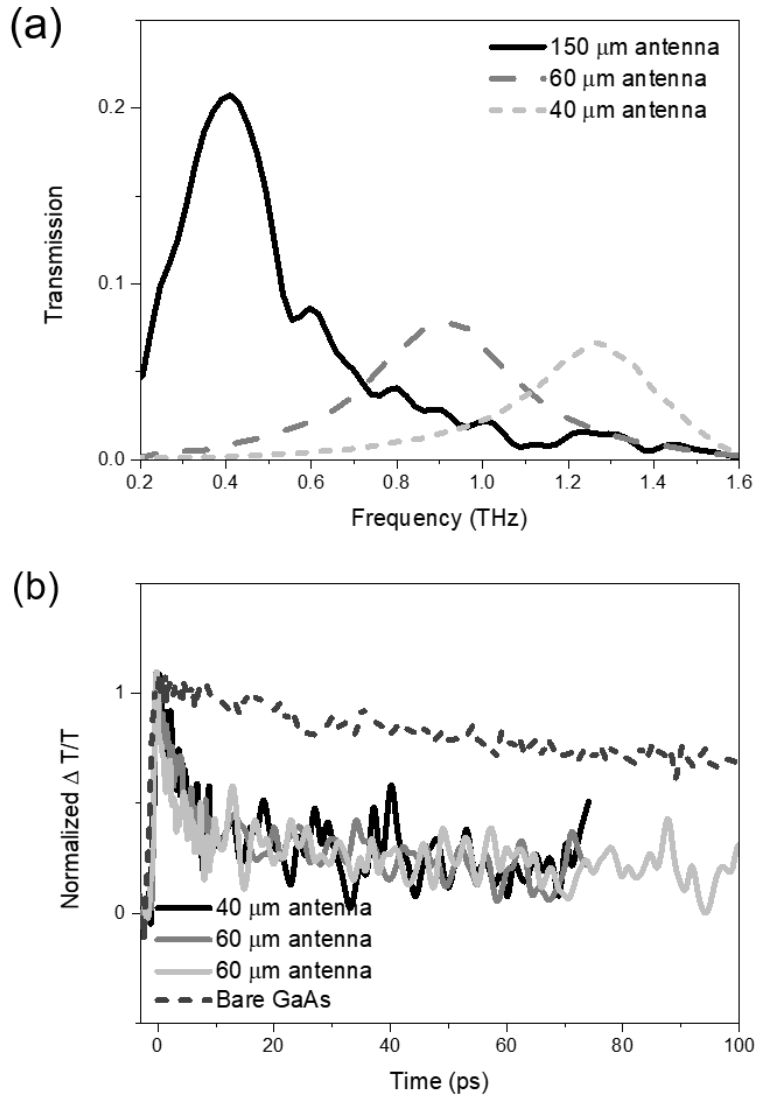

Fig. 5-11 (a) THz transmission for 150 μm length, 60 μm length, and 40 μm length antennas on GaAs substrate. The width of the antennas is fixed at 2 μm. Same as in Fig. 5-10, THz transmission increases for the longer length of antenna due to the larger field enhancement. (b) Normalized THz transmission changes for different length antenna samples. The carrier dynamics is faster than Fig. 5-8 (b) due to the field confinement to the surface. The optical pump power is 200 mW.

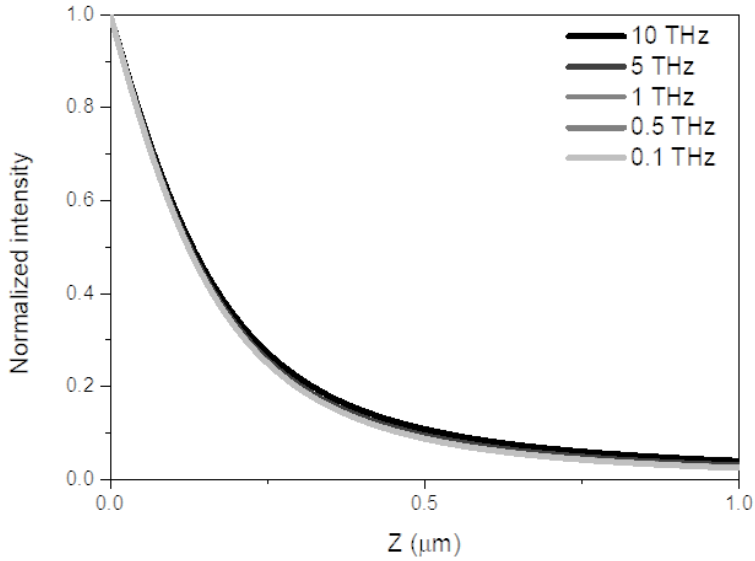

Fig. 5-12 Electric field intensity $|Ex|^2$ distribution of THz probe beam near 500 nm gap analytical calculations for different THz wavelengths.

Finally, we measured carrier dynamics for different optical pump powers (70 mW to 200 mW). Though the optical enhancement is marginal for our nanogap, it is important to measuring the carrier density effect, which can decrease carrier lifetime.[71-74] By considering optical field enhancement ($\sim$1) at the nanogap,[75,76] we increase the pump power up to 200 mW, which is three times larger than the original pump power of 70 mW. Figure 5-13 (a) shows that the carrier dynamics of bare InP are constant for the optical pump power up to the 200 mW. Furthermore, we measured carrier dynamics of 2 μm and 400 nm width antennas for different pump powers (Fig. 5-13 (b), (c)). The carrier dynamics of the nano antennas are also independent of pump power, showing that smaller confined depth (small width of antenna) effectively probes fast surface carrier dynamics. For GaAs substrate, the carrier dynamics of bare GaAs and antenna samples are constant for the optical pump power up to the 200 mW (Fig. 5-14). In addition to the experimental results, we calculated that the photoexcited carrier is below 5×10^{16} cm^{-3} for both InP and GaAs samples, which is low enough for linear THz response,[77] and the

optical pump is far away from the resonance of our antenna, thereby having no influence on spontaneous emission rate.[78]

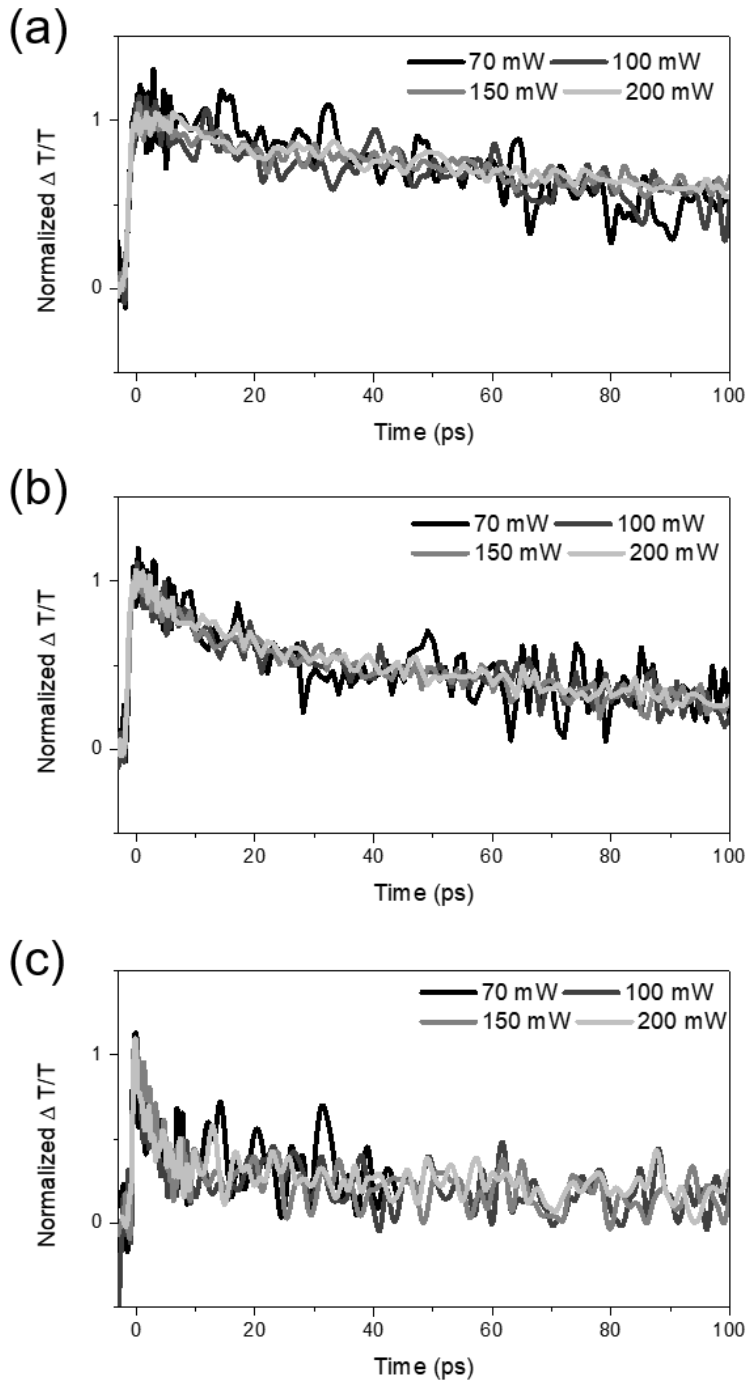

Fig. 5-13 Normalized THz transmission changes for (a) bare InP, (b) 2 μm, and (c) 400 nm metallic gap on InP substrate. The optical pump power is

changed from 70 mW to 200 mW.

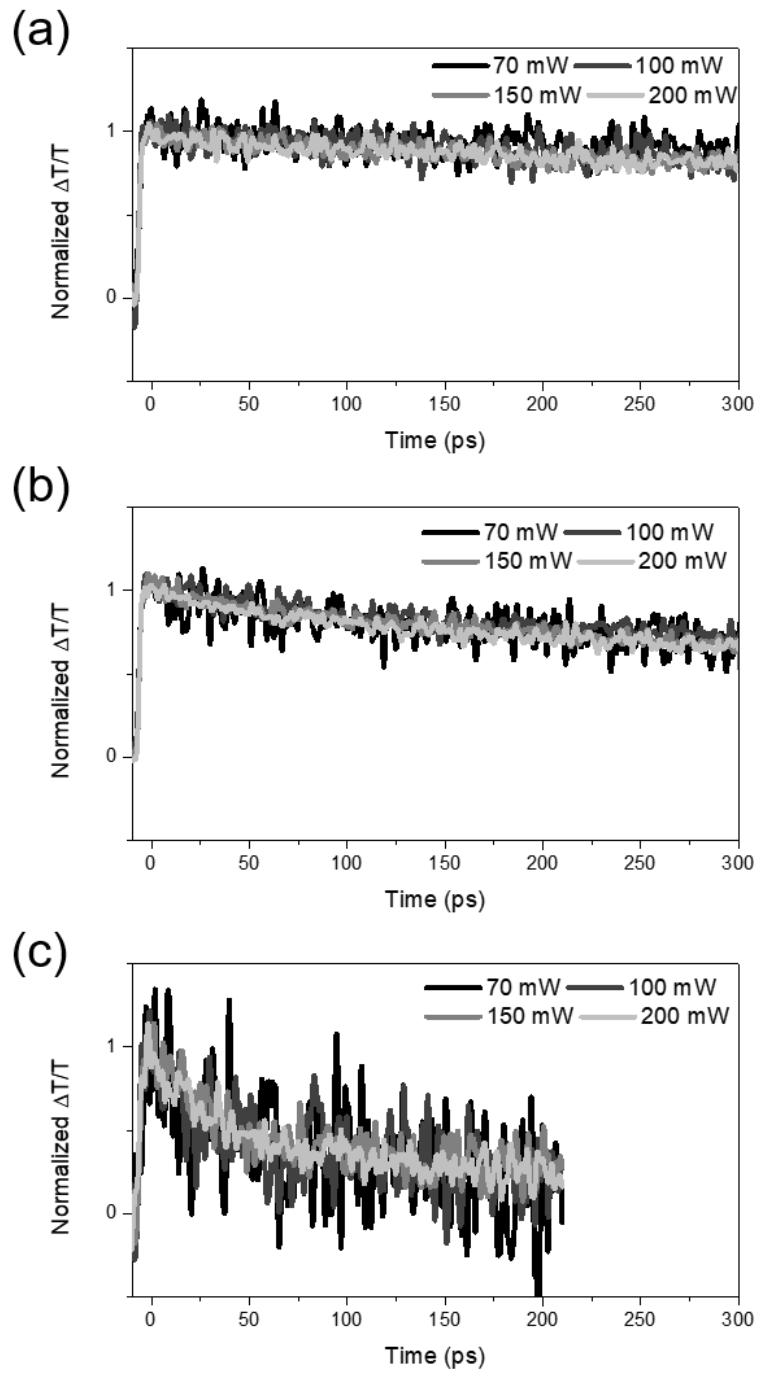

Fig. 5-14 Normalized THz transmission changes for (a) bare GaAs, (b) 2 μm, and (c) 400 nm metallic gap on GaAs substrate. The optical pump power is changed from 70 mW to 200 mW.

5.4 THz probe and optical pump field distribution near the gap

To take into account confined depth of the THz probe beam and effective penetration depth of the optical pump beam which play crucial roles in the measurements of surface carrier dynamics, we investigate near-field characteristics of electromagnetic waves for two different wavelengths (pump and probe). Electric intensity distribution $(|E_x|)^2$ of THz wave and optical power (P) are obtained from analytical calculation based on modal expansion and COMSOL simulation, respectively. As an example, in the 50 nm gap antenna, figure 5-15 shows electric intensity distribution $(|E_x|)^2$ of THz wave and optical power (P) for InP and GaAs, respectively. Generally, pump depth is smaller than the probe depth in the pump-probe experiment due to the high photon energy of pump beam. However, the THz probe beam has smaller depth than optical pump depth though its wavelength is 800 times larger than that of the pump beam due to the strong field confinement of THz wave (Fig. 5-15). THz probe beam therefore achieves the smaller spot size required by an ideal probe because the penetration into the sample can be described by the electrostatic leakage field of a parallel capacitor at length scale in orders of magnitude smaller than its wavelength.[33] The difference of pump depth between InP and GaAs is from the optical penetration depth of the semiconductor materials at 800 nm (Fig. 5-15 (b) and (d)).

We directly compared the normalized $|E_x|^2$ of THz probe beam (gray) and normalized P of optical pump beam (black) along the z-axis for 500 nm (top) and 50 nm (bottom) gap patterned on InP (left) and GaAs (right), respectively (Fig. 5-16). The different depth of pump or probe beam obviously indicates stronger field confinement for longer wavelength of electromagnetic waves ($\lambda_{pump} \sim$ 800 nm and $\lambda_{probe} \sim$ 600 μm). For the convenience, we define the effective probe depth of the confined THz probe

beam, d_{probe}, by full width at half-maximum (fwhm) of the THz electric intensity, while the effective pump depth of optical pump beam, d_{pump}, is defined by an effective penetration depth at which the optical power drops to 1/e from the surface value. Figure 5-17 is the summarization of d_{probe} and d_{pump} as a function of the gap size, showing that the confined probe depths of THz waves where the smallest gap is around 10 nm. With the increasing gap size, the confined depth of the THz probe beam linearly increases while the effective penetration depth of the pump beam increases and then saturates close to the penetration depth determined by the extinction coefficient of the materials at the wavelength of 800nm (d_{InP} ~ 300 nm and d_{GaAs} ~ 750 nm).

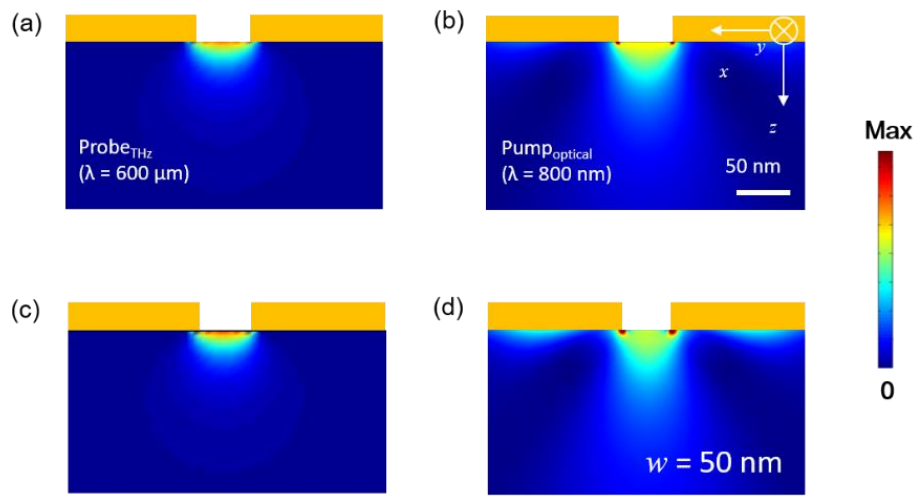

Fig. 5-15 Field distribution near 50 nm-sized nano-antenna on InP and GaAs substrate. Electric field intensity $|E_x|^2$ distribution of THz probe beam for (a) InP and (c) GaAs and Poynting vector |S| distribution of optical probe beam for (b) InP and (d) GaAs, obtained by analytical calculation based on modal expansion and COMSOL simulation, respectively.

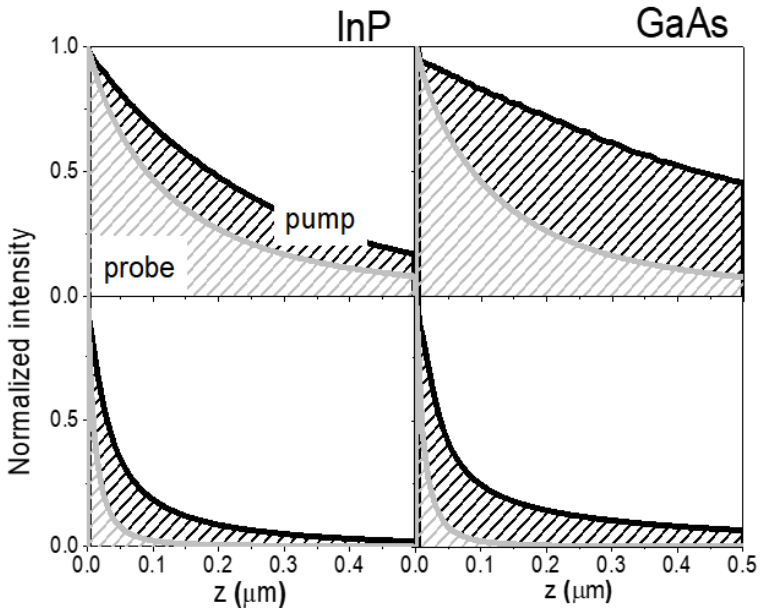

Fig. 5-16 Normalized $|E_x|^2$ of THz probe (black) and |S| of optical pump (gray) along the z-axis for 500 (top) and 50 (bottom) nm-antenna on InP (left) and GaAs (right), respectively. The different depth of pump and probe beam represents strong field confinement for THz probe beam.

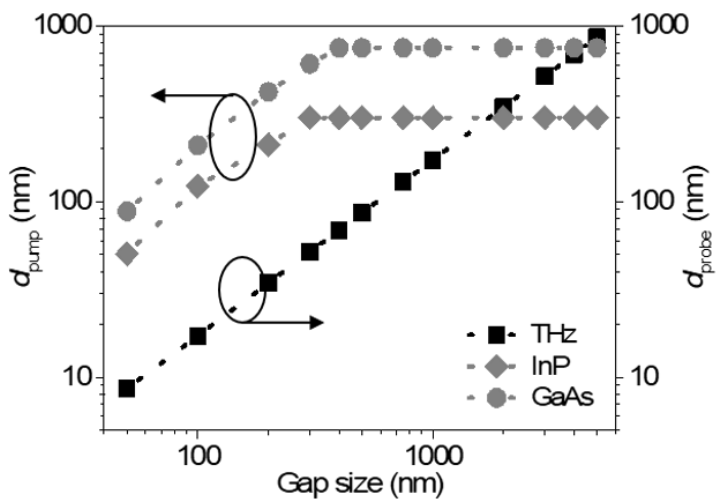

Fig. 5-17 Effective pump depth (d_{pump}) of optical pump beam for InP (diamond) and GaAs (circle) and effective probe depth (d_{probe}) of THz probe beam (square) as a function of the gap size.

5.5 Surface property analysis

With observation of surface carrier dynamics, it is important to analysis the surface property such as surface recombination velocity. To extract the surface recombination velocity from the nanoscopy method, we used carrier density distribution which is obtained by a one-dimensional diffusion equation, including bulk recombination and carrier excitation by the optical pump,[58,79]

$$\frac{\partial n(z,t)}{\partial t} = D\frac{\partial^2 n}{\partial z^2} - \frac{n}{\tau_b} + \delta(t)\exp(-\alpha z),$$

where n is the number of carriers at a distance z into the sample, D is the diffusion coefficient, τ_b is the bulk carrier lifetime, and α is the absorption coefficient of the optical pump. When we apply the boundary conditions;

$$n(0,t) = \frac{D}{S}\frac{\partial n(z,t)}{\partial t}\bigg|_{z=0}$$

$$n(l,t) = 0$$

$$n(z,0) = 0$$

where S is the surface recombination velocity and l is and arbitrarily long distance from the semiconductor surface at which the carrier density is zero for all time after carrier excitation. As a result, the carrier distribution is

$N(z,t) = n(z,t)\exp\left(-\frac{t^2}{\tau_b}\right)$, where

$$n(z,t) = \frac{1}{2}\exp\left(-\frac{z^2}{4Dt}\right)\times$$
$$\left[W\left(\alpha\sqrt{Dt} - \frac{z}{2\sqrt{Dt}}\right) - \frac{S+\alpha D}{S-\alpha D}W\left(\alpha\sqrt{Dt} + \frac{z}{2\sqrt{Dt}}\right) + \frac{2S}{S-\alpha D}W\left(S\sqrt{\frac{t}{D}} + \frac{z}{2\sqrt{Dt}}\right)\right]$$

and $w(\zeta) = \exp(\zeta^2)[1 - \mathrm{erf}(\zeta)]$. In particular, for applying nano-slot antenna samples, α is replaced with the effective absorption coefficient α_{eff} (= $1/d_{\mathrm{pump}}$). The values of α_{eff} for each nano-slot antenna sample are presented in Fig. 5-18, which is extracted from the effective optical pump depth (d_{pump}). We note that the penetration depths of bulk InP and GaAs are 300 nm (α = 33099 cm^{-1}) and 750 nm (α = 13455 cm^{-1}) at λ = 800 nm, respectively. When the gap size is larger than ~ 400 nm, the optical pump depth and the effective absorption coefficient are same with bulk characteristics. As the gap size decreases below 400 nm, however, the optical pump beam also starts to be confined with leading to a decrease of the effective optical pump depth linearly. As a result, the effective absorption coefficient is inversely proportional to the gap size and increases up to around 200000 cm^{-1} and 120000 cm^{-1} for 50 nm-antenna on the InP and GaAs substrate, respectively. Because the change of THz transmission is proportional to the number of the excited carriers as a function of time, integrated carriers in the effective probe depth represents the optical pump THz probe signal in experiment (Fig. 5-19). Therefore, for antenna samples, we integrate excited carriers from the surface to d_{probe} at each time delay. Figure 5-20 and 5-21 show normalized carrier density distributions for 500 nm- (top) and 50 nm-antenna (bottom) on InP and GaAs with specific *S* and *D* values, respectively. At each time delay, we integrated carrier densities from surface to effective probe depth (violet shade), which represents ΔT/T of the experimental data. Insets are integrated carrier densities as each time delay. To extract *S* and *D* from the experiment, we found *S* and *D* parameters that fit experimental results. As a result, the

obtained S and D values thus are $S = 1.5 \times 10^5$ cm/s, $D = 0.3$ cm^2 /s for InP; $S = 1.1 \times 10^6$ cm/s, $D = 45$ cm^2 /s for GaAs, which fit the experimental data very well (lines in Fig. 6-22). The S value of SI-InP is much larger than that reported for an intrinsic InP[62] but is similar to that reported for another semi-insulating InP result, $S = 1 \times 10^5$ cm/s.[64] For GaAs, the S value has consistent value with that in a previous work.[63] We note that, for these S and D values, carrier dynamics within the first few picoseconds is largely due to the surface recombination, while later dynamics is governed by diffusion and bulk recombination properties.[58] Therefore, a few picoseconds lifetime in the small nanogaps (in Fig. 5-22) represents observation of surface recombination by the effective THz probe depth smaller than pump depth.

Here, when we fit the experimental result, diffusion to the in-plane direction is neglected due to the much tighter confinement along the z-direction, compared with that along the x-direction. Strictly speaking, to analyze carrier dynamics, the in-plane diffusion should also be considered in carrier dynamics of our metal patterned semiconductor where the volume of photoexcitation is confined within a small region close to the surface. However, to simplify the calculation, we approximate the diffusion effect so as to concentrate mainly on the diffusion along the z-axis. Figure 5-23 presents an intensity distribution of the optical pump beam near the nano-slot antenna gap, showing that the carrier confinement is more severe along the z-direction compared with the x-direction, by about a factor of six if we measure the widths at 78% of the peak. This is related to the sub-wavelength nature of our gap, whereby confinement along the x-direction is sine-like but that along the z-direction is exponential-like. Therefore, diffusion along the z-direction is much more important than that along the x-direction if we assume that same diffusion constants for both directions.

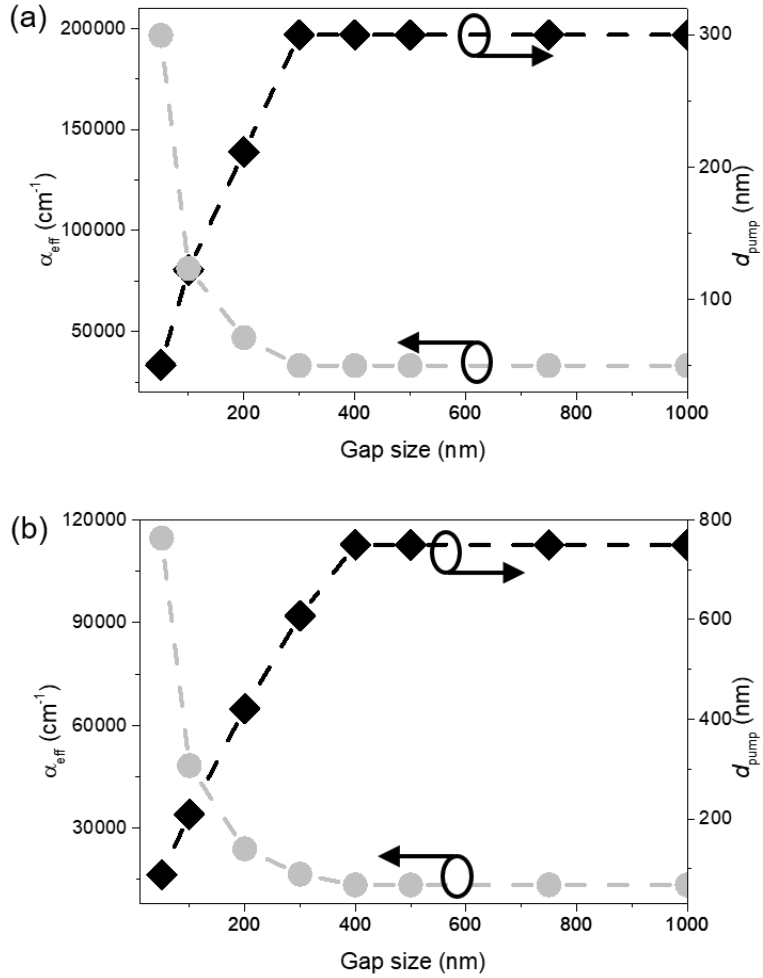

Fig. 5-18 effective optical pump depth (d_{pump}) and effective absorption coefficient (α_{eff}) dependent on gap size for InP (a) and GaAs (b).

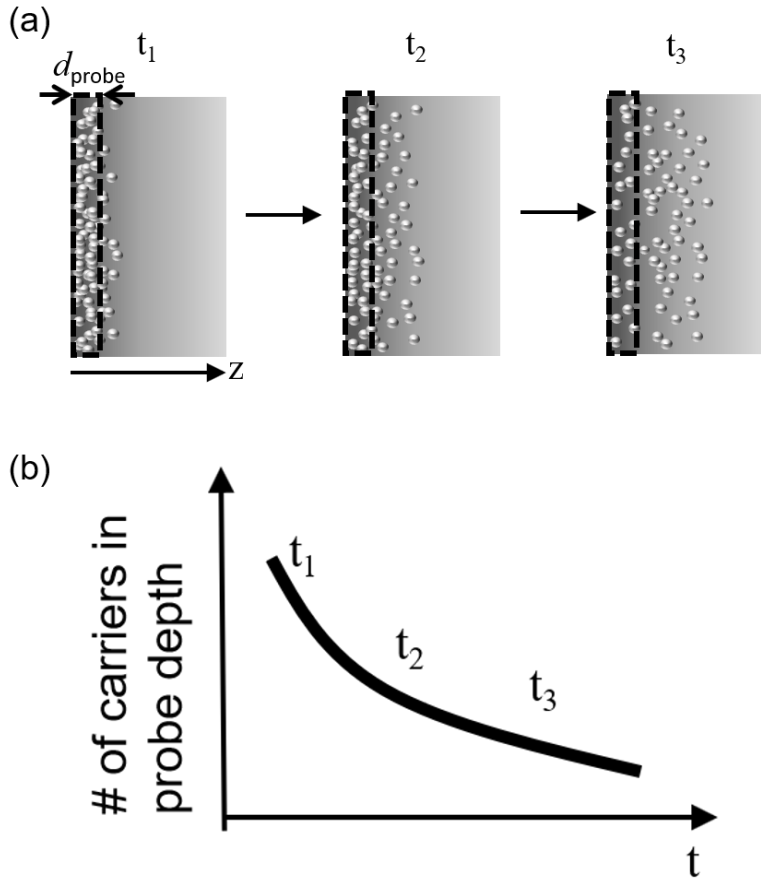

Fig. 5-19 (a) Schematic of carrier distribution as a function of time and position. (b) The number of carriers in the effective probe depth of (a) as a function of time.

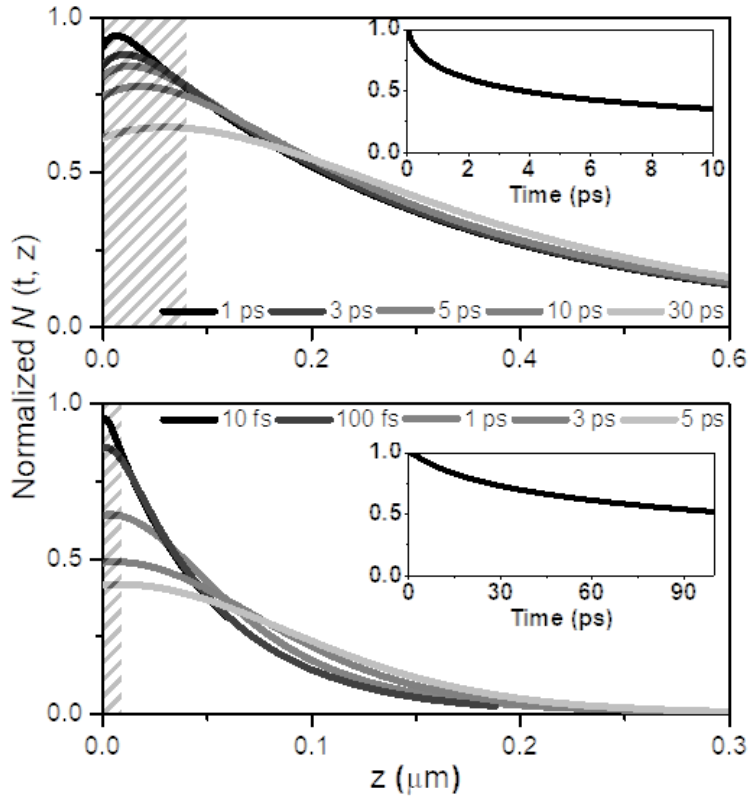

Fig. 5-20 Normalized carrier density distributions for 500 nm (top) and 50 nm (bottom) gap in InP substrate at various time delays. The shades represent the probe depth (d_{probe}) controlled by the THz confinement. The insets show normalized carrier density integrated from surface to d_{probe} as a function of time delay.

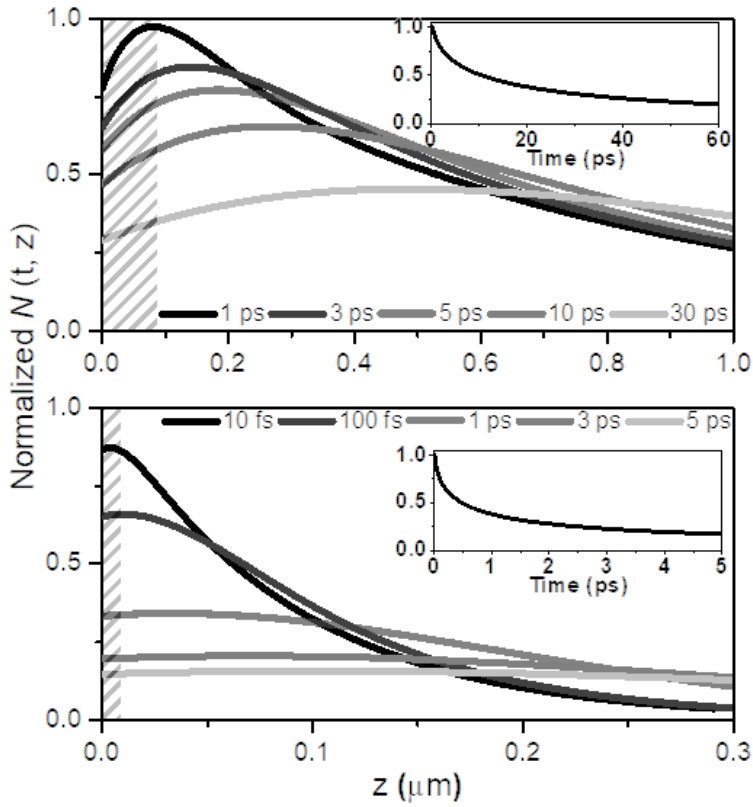

Fig. 5-21 Normalized carrier density distributions for 500 nm (top) and 50 nm (bottom) gap in GaAs substrate at various time delays. The shades represent the probe depth (d_{probe}) controlled by the THz confinement. The insets show normalized carrier density integrated from surface to d_{probe} as a function of time delay.

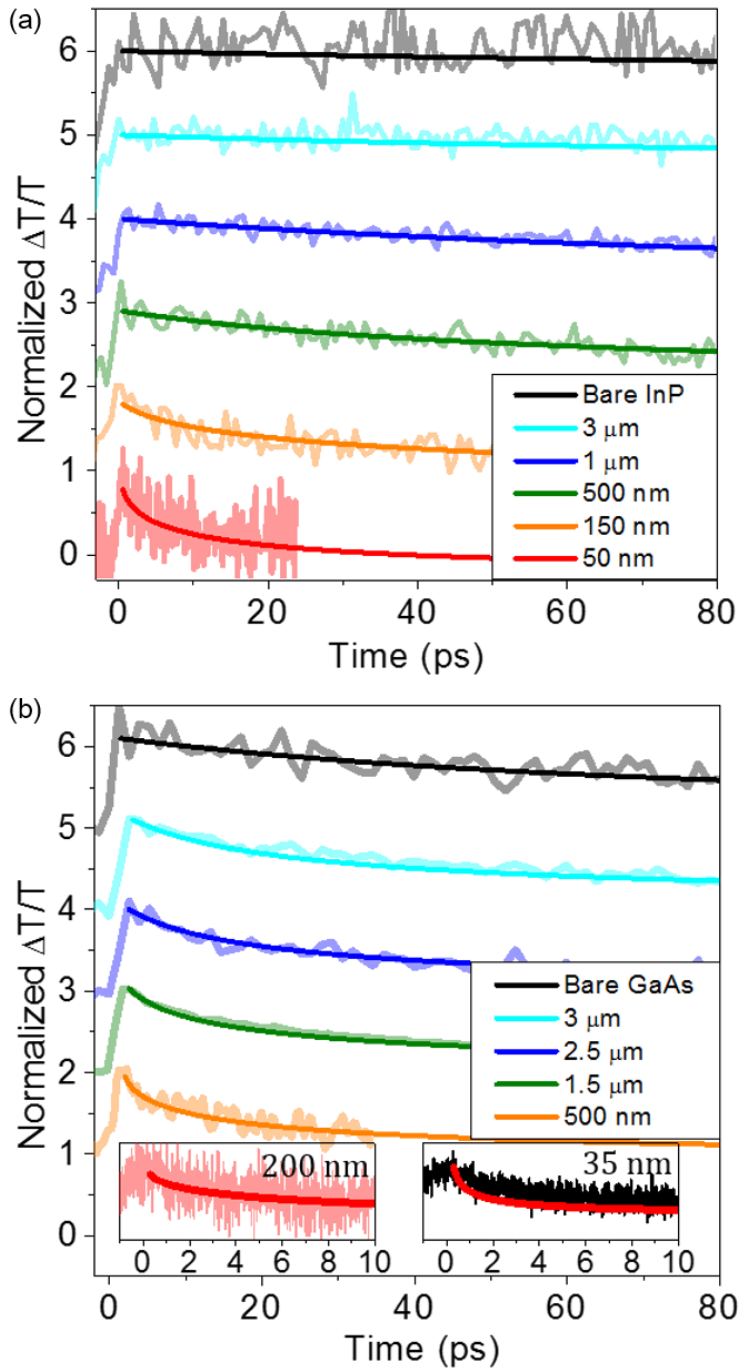

Fig. 5-22 Each fitting lines with experimental data are calculated by normalized carrier densities as a function of time. From the fitting, we extract the parameters $S = 1.5 \times 10^5$ cm/s, $D = 0.3$ cm^2/s for InP and $S = 1.1 \times 10^6$ cm/s, $D = 45$ cm^2/s for GaAs.

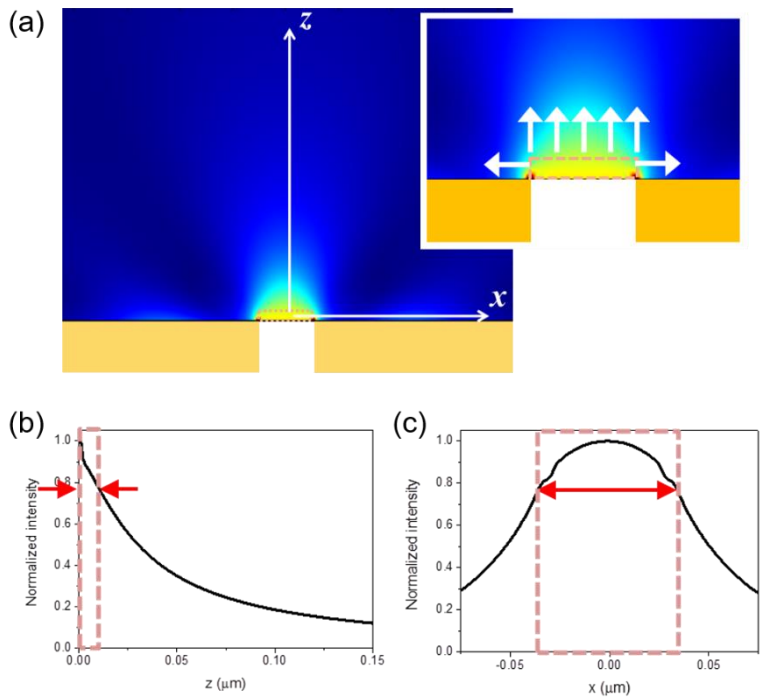

Fig. 5-23 (a) Intensity distribution of the optical pump beam for a 50 nm gap; COMSOL simulation. (b) and (c) Intensity profile along the z- and the x-direction, respectively. The dashed red line presents an effective photoexcitation area showing that the diffusion to z-direction is more dominant than x-direction.

Finally, in Figure 5-24, we plot the inverse of the carrier lifetime, $1/\tau$, for nano-slot antenna on InP and GaAs, as a function of the inverse of the effective probe depth, $1/d_{\text{probe}}$, controlled by the gap size. The carrier lifetimes (circular dot) are extracted by fitting the calculated lines in Fig. 5-22 with a single exponential function. As we decrease the gap size below 200 nm (50 nm), the carrier lifetime of GaAs (InP) dramatically decreases even below 1 ps, caused by surface state and surface defect driving the faster recombination process at the extreme surface of semiconductors. Though the carrier lifetime is saturate due to the time resolution limit in experiment, the figure shows that sub-pico carrier lifetime can be obtained and used from InP and GaAs by using nano-slot antenna. Our approach provides the most direct approach to the underlying surface dynamics of bulk semiconductors without inferring to nanostructures such as quantum wires or quantum wells. Moreover, with the help of nano-slot antenna patterning, the lifetimes of bulk semiconductor can be engineered with huge dynamic range, opening up new ultrafast optical applications.

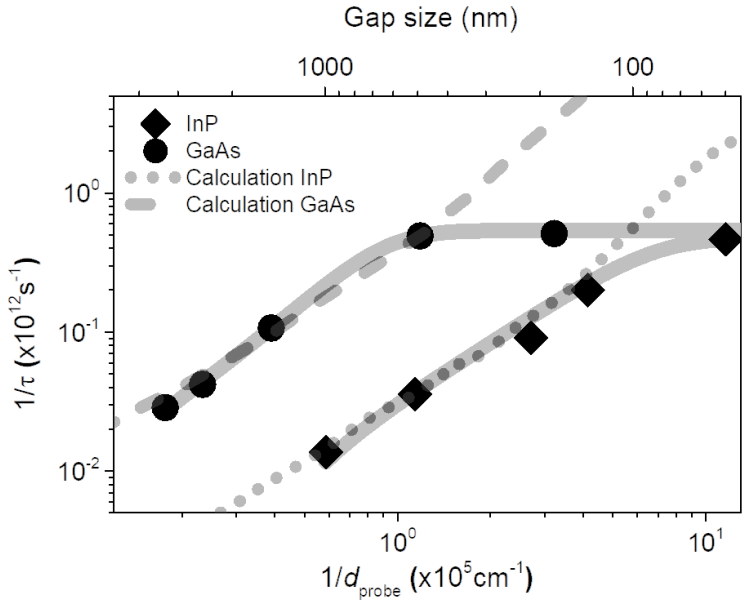

Fig. 5-24 Inverse of carrier lifetime ($1/\tau$) of nano-antenna on InP and GaAs as a function of the inverse of the effective probe depth ($1/d_{probe}$) controlled by the gap size. Carrier lifetimes are extracted from single exponential fits of experimental data and the fitted lines in Fig. 5-22. The solid lines are guide to the eye, which start to saturate around a recombination rate of 1/(2 ps) due to the limited time resolution of the setup.

Chapter 6. Conclusion

In conclusion, we demonstrated ultrafast surface dynamics measurements of bulk semiconductors (SI-InP and SI-GaAs) using THz nanoscopy antenna method. Taking advantage of the confined THz near-field, we can effectively measure the subliminal surface carrier dynamics for InP and GaAs, by confining both pump and probe beams spatially. The sample retains its original properties, as the complete restoration of bulk dynamics after removal of the nano-slot antenna patterns is demonstrated. By changing resonant frequency of antenna, we can choose the broad range of wavelength as a probe beam. Furthermore, we showed that the probe depth can be smaller than pump depth in nanoscopy antenna. This result represents that our THz nanoscopy antenna is another tool for probing semiconductor surface dynamics with several advantages such as non-destructive to semiconductor substrate, selection of the broad range of wavelength as a probe beam, and extreme small probe depth.

Through both experimental results and calculations, the surface recombination velocities and diffusion coefficients of the semiconductor materials were extracted. With ever decreasing the feature sizes we envision ultrafast switching applications using surface dynamics only, bypassing the much slower bulk dynamics.

Appendix

A.1 slit array -PEC

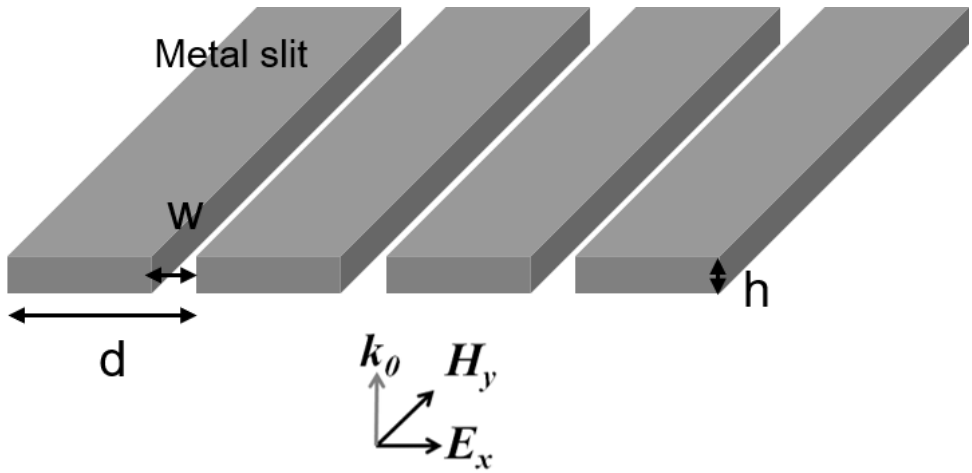

$$k_x^n = k_{0x} + \frac{2\pi n}{d},\quad k_{mz}^n = \pm\sqrt{\varepsilon_m k_0^2 - \left(k_x^n\right)^2},\quad m = I, III$$

$$\nabla\times\vec{H} = \frac{\partial\vec{D}}{\partial t} = -i\omega\varepsilon_0\varepsilon\vec{E} = -\frac{ik_0\varepsilon_0\varepsilon}{\varepsilon_0}\sqrt{\frac{\varepsilon_0}{\mu_0}}\vec{E},\quad \vec{E} = \frac{i}{k_0\varepsilon}\sqrt{\frac{\mu_0}{\varepsilon_0}}\nabla\times\vec{H}$$

(region I)

$$H_y^I = \sqrt{\frac{\varepsilon_0}{\mu_0}}\sum_n\left[\delta_{n0}e^{ik_{Iz}^n z} + g_n(k_x^n)e^{-ik_{Iz}^n z}\right]e^{ik_{Ix}^n x}$$

$$E_x^I = \frac{i}{k_0\varepsilon_I}\sqrt{\frac{\mu_0}{\varepsilon_0}}\left(\frac{\partial H_z}{\partial y} - \frac{\partial H_y}{\partial z}\right) = -\frac{i}{k_0\varepsilon_I}\sum_n\left[ik_{Iz}^n\delta_{n0}e^{ik_{Iz}^n z} - ik_{Iz}^n g_n(k_x^n)e^{-ik_{Iz}^n z}\right]e^{ik_x^n x}$$

$$E_z^I = \frac{i}{k_0\varepsilon_I}\sqrt{\frac{\mu_0}{\varepsilon_0}}\left(\frac{\partial H_y}{\partial x} - \frac{\partial H_x}{\partial y}\right) = \frac{i}{k_0\varepsilon_I}\sum_n ik_x^n\left[\delta_{n0}e^{ik_{Iz}^n z} + g_n(k_x^n)e^{-ik_{Iz}^n z}\right]e^{ik_x^n x}$$

(region III)

$$H_y^{III} = \sqrt{\frac{\varepsilon_0}{\mu_0}}\sum_n\left[f_n(k_x^n)e^{ik_{IIIx}^n x}e^{ik_{IIIz}^n(z-h)}\right]$$

$$E_x^{III} = \frac{i}{k_0 \varepsilon_{III}} \sqrt{\frac{\mu_0}{\varepsilon_0}} \left(\frac{\partial H_z}{\partial y} - \frac{\partial H_y}{\partial z} \right) = -\frac{i}{k_0 \varepsilon_{III}} \sum_n \left[ik_{IIIz}^n f_n(k_x^n) e^{ik_x^n x} e^{ik_{IIIz}^n (z-h)} \right]$$

$$E_z^{III} = \frac{i}{k_0 \varepsilon_{III}} \sqrt{\frac{\mu_0}{\varepsilon_0}} \left(\frac{\partial H_y}{\partial x} - \frac{\partial H_x}{\partial y} \right) = \frac{i}{k_0 \varepsilon_{III}} \sum_n \left[ik_x^n f_n(k_x^n) e^{ik_x^n x} e^{ik_{IIIz}^n (z-h)} \right]$$

(region II – single mode approximation)

$\beta = \sqrt{\varepsilon_{II} k_0^2}$: propagation constant of the fundamental TE mode

$$H_y^{II} = \begin{Bmatrix} \sqrt{\frac{\varepsilon_0}{\mu_0}} \left[A' e^{i\beta z} + B' e^{-i\beta z} \right] : -\frac{w}{2} < x < \frac{w}{2} \\ unknown : -\frac{d}{2} < x < -\frac{w}{2}, \frac{w}{2} < x < \frac{d}{2} \end{Bmatrix}$$

$$E_x^{II} = \begin{Bmatrix} \frac{i}{k_0 \varepsilon_{II}} \sqrt{\frac{\mu_0}{\varepsilon_0}} \left(\frac{\partial H_z}{\partial y} - \frac{\partial H_y}{\partial z} \right) \\ = \frac{\beta}{k_0 \varepsilon_{II}} \left[A' e^{i\beta z} - B' e^{-i\beta z} \right] = Ae^{i\beta z} + Be^{-i\beta z} : -\frac{w}{2} < x < \frac{w}{2} \\ 0 : -\frac{d}{2} < x < -\frac{w}{2}, \frac{w}{2} < x < \frac{d}{2} \end{Bmatrix}$$

<Boundary Condition>

	$z = 0$	$z = h$
$-\frac{w}{2} < x < \frac{w}{2}$	$H_y^I(z=0) = H_y^{II}(z=0)$ $\partial_z H_y^I(z=0) = \frac{\varepsilon_I}{\varepsilon_{II}} \partial_z H_y^{II}(z=0)$	$H_y^{III}(z=h) = H_y^{II}(z=h)$ $\partial_z H_y^{III}(z=h) = \frac{\varepsilon_{III}}{\varepsilon_{II}} \partial_z H_y^{II}(z=h)$
$-\frac{d}{2} < x < -\frac{w}{2}, \frac{w}{2} < x < \frac{d}{2}$	$\partial_z H_y^I(z=0) = 0$	$\partial_z H_y^{III}(z=h) = 0$

(1)

$$H_y^I(z=0) = H_y^{II}(z=0) : -\frac{w}{2} < x < \frac{w}{2}$$

$$\sqrt{\frac{\varepsilon_0}{\mu_0}}\sum_n\left[\delta_{n0}+g_n(k_x^n)\right]e^{ik_x^n x}=\sqrt{\frac{\varepsilon_0}{\mu_0}}\left[A'+B'\right]$$

multiply $\frac{1}{w}\int_{-\frac{w}{2}}^{\frac{w}{2}}dx$

$$\sum_n\left[\delta_{n0}+g_n(k_x^n)\right]\frac{1}{w}\int_{-\frac{w}{2}}^{\frac{w}{2}}dxe^{ik_x^n x}=\left[A'+B'\right]$$

$$\sum_n\left[\delta_{n0}+g_n(k_x^n)\right]J_n*=\left[A'+B'\right]$$

$$J_n*\equiv\frac{1}{w}\int_{-\frac{w}{2}}^{\frac{w}{2}}dxe^{ik_x^n x}=\sin c\left(\frac{k_x^n w}{2}\right)$$

(2)

$$\partial_z H_y^I(z=0)=\begin{cases}\frac{\varepsilon_I}{\varepsilon_{II}}\partial_z H_y^{II}(z=0):-\frac{w}{2}<x<\frac{w}{2}\\ 0:-\frac{d}{2}<x<-\frac{w}{2},\frac{w}{2}<x<\frac{d}{2}\end{cases}$$

$$\sum_n\left[ik_{Iz}^n\delta_{n0}-ik_{Iz}^n g_n(k_x^n)\right]e^{ik_x^n x}=\begin{cases}\frac{\varepsilon_I}{\varepsilon_{II}}i\beta\left[A'-B'\right]:-\frac{w}{2}<x<\frac{w}{2}\\ 0:-\frac{d}{2}<x<-\frac{w}{2},\frac{w}{2}<x<\frac{d}{2}\end{cases}$$

Multiply $e^{-ik_x^{n'}x}$ and $\frac{1}{d}\int_{-\frac{d}{2}}^{\frac{d}{2}}dx$

$$\left[ik_{Iz}^{n'}\delta_{n'0}-ik_{Iz}^{n'}g_{n'}(k_x^{n'})\right]=\frac{\varepsilon_I}{\varepsilon_{II}}i\beta\left[A'-B'\right]\frac{1}{d}\int_{-\frac{w}{2}}^{\frac{w}{2}}dxe^{-ik_x^{n'}x}$$

$$g_n(k_x^n)=\delta_{n0}-\frac{\varepsilon_I}{\varepsilon_{II}}\frac{\beta}{k_{Iz}^n}\left[A'-B'\right]\frac{w}{d}J_n$$

$$J_n\equiv\frac{1}{w}\int_{-\frac{w}{2}}^{\frac{w}{2}}dxe^{-ik_x^n x}=\sin c\left(\frac{k_x^n w}{2}\right)$$

(3)

$$H_y^{III}(z=h)=H_y^{II}(z=h):-\frac{w}{2}<x<\frac{w}{2}$$

$$\sqrt{\frac{\varepsilon_0}{\mu_0}}\sum_n\left[f_n(k_x^n)e^{ik_x^n x}\right]=\sqrt{\frac{\varepsilon_0}{\mu_0}}\left[A'e^{i\beta h}+B'e^{-i\beta h}\right]$$

multiply $\int_{-\frac{w}{2}}^{\frac{w}{2}}dx$

$$\sum_n f_n(k_x^n)J_n*=\left[A'e^{i\beta h}+B'e^{-i\beta h}\right]$$

(4)

$$\partial_z H_y^{III}(z=h)=\begin{cases}\frac{\varepsilon_{III}}{\varepsilon_{II}}\partial_z H_y^{II}(z=h):-\frac{w}{2}<x<\frac{w}{2}\\ 0:-\frac{d}{2}<x<-\frac{w}{2},\frac{w}{2}<x<\frac{d}{2}\end{cases}$$

$$\sum_n ik_{IIIz}^n f_n(k_x^n)e^{ik_x^n x}=\left\{\begin{array}{c}\frac{\varepsilon_{III}}{\varepsilon_{II}}i\beta\left[A'e^{i\beta h}-B'e^{-i\beta h}\right]:-\frac{w}{2}<x<\frac{w}{2}\\ 0:-\frac{d}{2}<x<-\frac{w}{2},\frac{w}{2}<x<\frac{d}{2}\end{array}\right\}$$

Multiply $e^{-ik_x^{n'}x}$ and $\frac{1}{d}\int_{-\frac{d}{2}}^{\frac{d}{2}}dx$

$$ik_{IIIz}^{n'}f_{n'}(k_x^{n'})=\frac{\varepsilon_{III}}{\varepsilon_{II}}i\beta\left[A'e^{i\beta h}-B'e^{-i\beta h}\right]\frac{1}{d}\int_{-\frac{w}{2}}^{\frac{w}{2}}dxe^{-ik_x^{n'}x}$$

$$f_n(k_x^n)=\frac{\varepsilon_{III}}{\varepsilon_{II}}\frac{\beta}{k_{IIIz}^n}\left[A'e^{i\beta h}-B'e^{-i\beta h}\right]\frac{w}{d}J_n$$

(2) is substituted into (1)

$$\sum_n\left[2\delta_{n0}-\frac{\varepsilon_I}{\varepsilon_{II}}\frac{\beta}{k_{Iz}^n}\left[A'-B'\right]\frac{w}{d}J_n\right]J_n*=\left[A'+B'\right]$$

->(5) $2J_0*-\sum_n\frac{\varepsilon_I}{\varepsilon_{II}}\frac{\beta}{k_{Iz}^n}\frac{w}{d}J_nJ_n*\left[A'-B'\right]=\left[A'+B'\right]$

(4) is substituted into (3)

$$\sum_n \frac{\varepsilon_{III}}{\varepsilon_{II}} \frac{\beta}{k_{IIIz}^n} \left[A' e^{i\beta h} - B' e^{-i\beta h}\right] \frac{w}{d} J_n J_n * = \left[A' e^{i\beta h} + B' e^{-i\beta h}\right]$$

->(6) $$\sum_n \frac{\varepsilon_{III}}{\varepsilon_{II}} \frac{\beta}{k_{IIIz}^n} \frac{w}{d} J_n J_n * \left[A' e^{i\beta h} - B' e^{-i\beta h}\right] = \left[A' e^{i\beta h} + B' e^{-i\beta h}\right]$$

$$E \equiv \frac{E_{in}}{E_{0air}} = \frac{\frac{\beta}{k_0 \varepsilon_{II}} \left[A' - B'\right]}{1} = \frac{\beta}{k_0 \varepsilon_{II}} \left[A' - B'\right] = \left[A + B\right]$$

$$A = \frac{\beta}{k_0 \varepsilon_{II}} A', \quad B = -\frac{\beta}{k_{0z} \varepsilon_{II}} B'$$

$$E' \equiv -\frac{E_{out}}{E_{0air}} = -\frac{\frac{\beta}{k_0 \varepsilon_{//}} \left[A' e^{j\beta h} - B' e^{-j\beta h}\right]}{1}$$

$$= -\frac{\beta}{k_{0₩} \varepsilon_{//}} \left[A' e^{j\beta h} - B' e^{-j\beta h}\right] = -\left[A e^{j\beta h} + B e^{-j\beta h}\right]$$

$$A' = \frac{k_0 \varepsilon_{II}}{\beta} \frac{-E' - E e^{-i\beta h}}{2i \sin(\beta h)}, \quad B' = -\frac{k_0 \varepsilon_{II}}{\beta} \frac{E' + E e^{i\beta h}}{2i \sin(\beta h)}$$

$$A' - B' = \frac{k_0 \varepsilon_{II}}{\beta} E$$

$$A' + B' = \frac{k_0 \varepsilon_{//}}{\beta} \left[\frac{-E' - E e^{-i\beta h}}{2i \sin(\beta h)} - \frac{E' + E e^{j\beta h}}{2i \sin(\beta h)}\right]$$

$$= i \frac{k_0 \varepsilon_{//}}{\beta} \left[\frac{E' + \cos(\beta h) E}{\sin(\beta h)}\right] = i \frac{k_0 \varepsilon_{//}}{\beta} \left[\frac{E' + \cos(\beta h) E}{\sin(\beta h)}\right]$$

$$A' e^{i\beta h} - B' e^{-i\beta h} = -\frac{k_0 \varepsilon_{II}}{\beta} E'$$

$$A'e^{i\beta h}+B'e^{-i\beta h}=\frac{k_0\varepsilon_{//}}{\beta}\left[\frac{-E'-Ee^{-i\beta h}}{2i\sin(\beta h)}e^{i\beta h}-\frac{E'+Ee^{i\beta h}}{2i\sin(\beta h)}e^{-i\beta h}\right]$$

$$=i\frac{k_0\varepsilon_{//}}{\beta}\frac{E'\cos(\beta h)+E}{\sin(\beta h)}$$

(5) $$2J_0*-\sum_n\frac{\varepsilon_I}{\varepsilon_{II}}\frac{\beta}{k_{Iz}^n}\frac{w}{d}J_nJ_n*\left[A'-B'\right]=\left[A'+B'\right]$$

$$2J_0*-\sum_n\frac{\varepsilon_I}{\varepsilon_{II}}\frac{\beta}{k_{Iz}^n}\frac{w}{d}J_nJ_n*\frac{k_0\varepsilon_{II}}{\beta}E=i\frac{k_0\varepsilon_{II}}{\beta}\left[\frac{E'+\cos(\beta h)E}{\sin(\beta h)}\right]$$

(6) $$\sum_n\frac{\varepsilon_{III}}{\varepsilon_{II}}\frac{\beta}{k_{IIIz}^n}\frac{w}{d}J_nJ_n*\left[A'e^{i\beta h}-B'e^{-i\beta h}\right]=\left[A'e^{i\beta h}+B'e^{-i\beta h}\right]$$

$$-\sum_n\frac{\varepsilon_{III}}{\varepsilon_{II}}\frac{\beta}{k_{IIIz}^n}\frac{w}{d}J_nJ_n*\frac{k_0\varepsilon_{II}}{\beta}E'=i\frac{k_0\varepsilon_{II}}{\beta}\frac{E'\cos(\beta h)+E}{\sin(\beta h)}$$

$$\left[i\sum_n\frac{k_0\varepsilon_I}{k_{Iz}^n}\frac{w}{d}J_nJ_n*-\frac{\frac{k_0\varepsilon_{II}}{\beta}}{\tan(\beta h)}\right]E-\frac{\frac{k_0\varepsilon_{II}}{\beta}}{\sin(\beta h)}E'=2i\sin c\left(\frac{\sqrt{\varepsilon_I}k_{0x}w}{2}\right)$$

$$-\frac{\frac{k_0\varepsilon_{II}}{\beta}}{\sin(\beta h)}E+\left[i\sum_n\frac{k_0\varepsilon_{III}}{k_{IIIz}^n}\frac{w}{d}J_nJ_n*-\frac{\frac{k_0\varepsilon_{II}}{\beta}}{\tan(\beta h)}\right]E'=0$$

$$G^{I,III}\equiv i\frac{w}{d}\sum_n\frac{k_0\varepsilon_{I,III}}{k_{I,IIIz}^n}J_nJ_n*=i\frac{w}{d}\sum_n\frac{k_0\varepsilon_{I,III}}{k_{I,IIIz}^n}\sin c^2\left(\frac{k_{I,IIIx}^n w}{2}\right)$$

$$\Sigma\equiv\frac{\frac{k_0\varepsilon_{II}}{\beta}}{\tan(\beta h)}=\frac{\frac{\beta}{k_0}}{\tan(\beta h)}$$

$$G_V\equiv\frac{\frac{k_0\varepsilon_{II}}{\beta}}{\sin(\beta h)}=\frac{\frac{\beta}{k_0}}{\sin(\beta h)}$$

$$I_0 \equiv 2i \sin c\left(\frac{\sqrt{\varepsilon_I}k_{0x}w}{2}\right)$$

$$\left(G^I - \Sigma\right)E - G_V E' = I_0$$
$$-G_V E + \left(G^{III} - \Sigma\right)E' = 0$$

$$\begin{bmatrix} G^I - \Sigma & -G_V \\ -G_V & G^{III} - \Sigma \end{bmatrix}\begin{bmatrix} E \\ E' \end{bmatrix} = \begin{bmatrix} I_0 \\ 0 \end{bmatrix}$$

$$\begin{bmatrix} E \\ E' \end{bmatrix} = \frac{I_0}{\left(G^I - \Sigma\right)\left(G^{III} - \Sigma\right) - \left(G_V\right)^2}\begin{bmatrix} G^{III} - \Sigma \\ G_V \end{bmatrix}$$

Bibliography

1 Dawlaty, J. M., Shivaraman, S., Chandrashekhar, M., Rana, F. & Spencer, M. G. Measurement of ultrafast carrier dynamics in epitaxial graphene. *Applied Physics Letters* **92**, 042116, doi:10.1063/1.2837539 (2008).

2 Zhang, W. *et al.* Carrier Recombination Dynamics in Sulfur-Doped InP Nanowires. *Nano Letters* **15**, 7238-7244, doi:10.1021/acs.nanolett.5b02022 (2015).

3 Kar, A. *et al.* Probing Ultrafast Carrier Dynamics in Silicon Nanowires. *IEEE Journal of Selected Topics in Quantum Electronics* **17**, 889-895, doi:10.1109/JSTQE.2010.2076399 (2011).

4 Prasankumar, R. P., Choi, S., Trugman, S. A., Picraux, S. T. & Taylor, A. J. Ultrafast Electron and Hole Dynamics in Germanium Nanowires. *Nano Letters* **8**, 1619-1624, doi:10.1021/nl080202+ (2008).

5 Cho, Y.-H. *et al.* Dynamics of anti-Stokes photoluminescence in type-II ${\mathrm{Al}}_{x}{\mathrm{Ga}}_{1\ensuremath{-}x}{\mathrm{As}\ensuremath{-}\mathrm{G}\mathrm{a}\mathrm{I}\mathrm{n}\mathrm{P}}_{2}$ heterostructures: The important role of long-lived carriers near the interface. *Physical Review B* **56**, R4375-R4378 (1997).

6 Yong, C. K. *et al.* Strong Carrier Lifetime Enhancement in GaAs Nanowires Coated with Semiconducting Polymer. *Nano Letters* **12**, 6293-6301, doi:10.1021/nl3034027 (2012).

7 Halas, N. J. & Bokor, J. Surface Recombination on the Si(111) 2\ifmmode\times\else\texttimes\fi{}1 Surface. *Physical Review Letters* **62**, 1679-1682 (1989).

8 Motet, T., Nees, J., Williamson, S. & Mourou, G. 1.4 ps rise-time high-voltage photoconductive switching. *Applied Physics Letters* **59**,

1455-1457, doi:10.1063/1.105286 (1991).

9 Krotkus, A. *et al.* Subpicosecond carrier lifetimes in GaAs grown by molecular beam epitaxy at low substrate temperature. *Applied Physics Letters* **66**, 1939-1941, doi:10.1063/1.113283 (1995).

10 Somma, C., Reimann, K., Flytzanis, C., Elsaesser, T. & Woerner, M. High-Field Terahertz Bulk Photovoltaic Effect in Lithium Niobate. *Physical Review Letters* **112**, 146602 (2014).

11 Parkinson, P. *et al.* Transient Terahertz Conductivity of GaAs Nanowires. *Nano Letters* **7**, 2162-2165, doi:10.1021/nl071162x (2007).

12 Li, M. *et al.* Size and surface effects on transient photoconductivity in CdS nanobelts probed by time-resolved terahertz spectroscopy. *Applied Physics Letters* **101**, 091104, doi:10.1063/1.4748300 (2012).

13 Calarco, R. *et al.* Size-dependent Photoconductivity in MBE-Grown GaN−Nanowires. *Nano Letters* **5**, 981-984, doi:10.1021/nl0500306 (2005).

14 Leitenstorfer, A. *et al.* Femtosecond Carrier Dynamics in GaAs Far from Equilibrium. *Physical Review Letters* **76**, 1545-1548 (1996).

15 Hatami, F. *et al.* Carrier dynamics in type-II GaSb/GaAs quantum dots. *Physical Review B* **57**, 4635-4641 (1998).

16 Becker, P. C. *et al.* Femtosecond Photon Echoes from Band-to-Band Transitions in GaAs. *Physical Review Letters* **61**, 1647-1649 (1988).

17 Yee, K. J., Lim, Y. S., Dekorsy, T. & Kim, D. S. Mechanisms for the Generation of Coherent Longitudinal-Optical Phonons in GaAs $/$AlGaAs Multiple Quantum Wells. *Physical Review Letters* **86**, 1630-1633 (2001).

18 Lui, K. P. H. & Hegmann, F. A. Ultrafast carrier relaxation in radiation-damaged silicon on sapphire studied by optical-pump–terahertz-probe experiments. *Applied Physics Letters* **78**, 3478-3480, doi:10.1063/1.1375841 (2001).

19 Ulbricht, R., Hendry, E., Shan, J., Heinz, T. F. & Bonn, M. Carrier dynamics in semiconductors studied with time-resolved terahertz spectroscopy. *Reviews of Modern Physics* **83**, 543-586 (2011).

20 Bjarnason, J. E., Chan, T. L. J., Lee, A. W. M., Celis, M. A. & Brown, E. R. Millimeter-wave, terahertz, and mid-infrared transmissionthrough common clothing. *Applied Physics Letters* **85**, 519-521, doi:10.1063/1.1771814 (2004).

21 Jördens, C., Wietzke, S., Scheller, M. & Koch, M. Investigation of the water absorption in polyamide and wood plastic composite by terahertz time-domain spectroscopy. *Polymer Testing* **29**, 209-215, doi:https://doi.org/10.1016/j.polymertesting.2009.11.003 (2010).

22 Shen, Y. C. *et al.* Detection and identification of explosives using terahertz pulsed spectroscopic imaging. *Applied Physics Letters* **86**, 241116, doi:10.1063/1.1946192 (2005).

23 Hu, Y., Huang, P., Guo, L., Wang, X. & Zhang, C. Terahertz spectroscopic investigations of explosives. *Physics Letters A* **359**, 728-732, doi:https://doi.org/10.1016/j.physleta.2006.07.046 (2006).

24 Davies, A. G., Burnett, A. D., Fan, W., Linfield, E. H. & Cunningham, J. E. Terahertz spectroscopy of explosives and drugs. *Materials Today* **11**, 18-26, doi:https://doi.org/10.1016/S1369-7021(08)70016-6 (2008).

25 Taylor, Z. D. *et al.* Reflective terahertz imaging of porcine skin burns. *Opt. Lett.* **33**, 1258-1260, doi:10.1364/OL.33.001258 (2008).

26 Woodward, R. M., Wallace, V. P., Arnone, D. D., Linfield, E. H. & Pepper, M. Terahertz Pulsed Imaging of Skin Cancer in the Time and Frequency Domain. *Journal of Biological Physics* **29**, 257-259, doi:10.1023/a:1024409329416 (2003).

27 Murrill, S. R. *et al.* Terahertz imaging system performance model for concealed-weapon identification. *Appl. Opt.* **47**, 1286-1297, doi:10.1364/AO.47.001286 (2008).

28 Kim, G.-J. *et al.* Enhanced Continuous-Wave Terahertz Imaging with a Horn Antenna for Food Inspection. *Journal of Infrared, Millimeter, and Terahertz Waves* **33**, 657-664, doi:10.1007/s10762-012-9902-1 (2012).

29 Roehle, H. *et al.* Next generation 1.5 μm terahertz antennas:  mesa-structuring of  InGaAs/InAlAs photoconductive layers. *Opt. Express* **18**, 2296-2301, doi:10.1364/OE.18.002296 (2010).

30 Yeh, K.-L., Hebling, J., Hoffmann, M. C. & Nelson, K. A. Generation of high average power 1kHz shaped THz pulses via optical rectification. *Optics Communications* **281**, 3567-3570, doi:https://doi.org/10.1016/j.optcom.2008.03.018 (2008).

31 Johnston, M. B., Whittaker, D. M., Corchia, A., Davies, A. G. & Linfield, E. H. Simulation of terahertz generation at semiconductor surfaces. *Physical Review B* **65**, 165301 (2002).

32 Duvillaret, L., Garet, F., Roux, J. F. & Coutaz, J. L. Analytical modeling and optimization of terahertz time-domain spectroscopy experiments, using photoswitches as antennas. *IEEE Journal of Selected Topics in Quantum Electronics* **7**, 615-623, doi:10.1109/2944.974233 (2001).

33 Seo, M. A. *et al.* Terahertz field enhancement by a metallic nano slit operating beyond the skin-depth limit. *Nat Photon* **3**, 152-156 (2009).

34 Toma, A. *et al.* Squeezing Terahertz Light into Nanovolumes: Nanoantenna Enhanced Terahertz Spectroscopy (NETS) of Semiconductor Quantum Dots. *Nano Letters* **15**, 386-391, doi:10.1021/nl503705w (2015).

35 Yang, Y., Singh, R. & Zhang, W. Anomalous terahertz transmission in bow-tie plasmonic antenna apertures. *Opt. Lett.* **36**, 2901-2903, doi:10.1364/OL.36.002901 (2011).

36 Park, D. J. *et al.* Terahertz near-field enhancement in narrow

rectangular apertures on metal film. *Opt. Express* **17**, 12493-12501, doi:10.1364/OE.17.012493 (2009).

37 Webb, K. J. & Li, J. Analysis of transmission through small apertures in conducting films. *Physical Review B* **73**, 033401 (2006).

38 García de Abajo, F. J. Light transmission through a single cylindrical hole in a metallic film. *Opt. Express* **10**, 1475-1484, doi:10.1364/OE.10.001475 (2002).

39 Lezec, H. J. *et al.* Beaming Light from a Subwavelength Aperture. *Science* **297**, 820-822, doi:10.1126/science.1071895 (2002).

40 de Abajo, F. J. G. I. Light transmission through a single cylindrical hole in a metallic film. *Optics Express* **10**, 1475-1484 (2002).

41 Fromm, D. P., Sundaramurthy, A., Schuck, P. J., Kino, G. & Moerner, W. E. Gap-Dependent Optical Coupling of Single "Bowtie" Nanoantennas Resonant in the Visible. *Nano Letters* **4**, 957-961, doi:10.1021/nl049951r (2004).

42 Kirchain, R. & Kimerling, L. A roadmap for nanophotonics. *Nature Photonics* **1**, 303, doi:10.1038/nphoton.2007.84 (2007).

43 Schuller, J. A. *et al.* Plasmonics for extreme light concentration and manipulation. *Nature Materials* **9**, 193, doi:10.1038/nmat2630 (2010).

44 Kauranen, M. & Zayats, A. V. Nonlinear plasmonics. *Nature Photonics* **6**, 737, doi:10.1038/nphoton.2012.244 (2012).

45 Bahk, Y.-M. *et al.* Electromagnetic Saturation of Angstrom-Sized Quantum Barriers at Terahertz Frequencies. *Physical Review Letters* **115**, 125501 (2015).

46 Jeong, J., Rhie, J., Jeon, W., Hwang, C. S. & Kim, D.-S. High-throughput fabrication of infinitely long 10 nm slit arrays for terahertz applications. *Journal of Infrared, Millimeter, and Terahertz Waves* **36**, 262-268, doi:10.1007/s10762-014-0135-3 (2015).

47 Chen, X. *et al.* Atomic layer lithography of wafer-scale nanogap arrays for extreme confinement of electromagnetic waves. **4**, 2361,

doi:10.1038/ncomms3361
https://www.nature.com/articles/ncomms3361#supplementary-information (2013).

48 Park, H.-R. *et al.* Colossal Absorption of Molecules Inside Single Terahertz Nanoantennas. *Nano Letters* **13**, 1782-1786, doi:10.1021/nl400374z (2013).

49 Jeong, Y.-G. *et al.* Large enhancement of nonlinear terahertz absorption in intrinsic GaAs by plasmonic nano antennas. *Applied Physics Letters* **103**, 171109, doi:10.1063/1.4826272 (2013).

50 Jeong, Y.-G. *et al.* A Vanadium Dioxide Metamaterial Disengaged from Insulator-to-Metal Transition. *Nano Letters* **15**, 6318-6323, doi:10.1021/acs.nanolett.5b02361 (2015).

51 Choi, S. B. *et al.* Nanopattern enabled terahertz all-optical switching on vanadium dioxide thin film. *Applied Physics Letters* **98**, 071105, doi:10.1063/1.3553504 (2011).

52 Kim, J.-Y. *et al.* Terahertz Quantum Plasmonics of Nanoslot Antennas in Nonlinear Regime. *Nano Letters* **15**, 6683-6688, doi:10.1021/acs.nanolett.5b02505 (2015).

53 Choe, J.-H., Kang, J.-H., Kim, D.-S. & Park, Q. H. Slot antenna as a bound charge oscillator. *Opt. Express* **20**, 6521-6526, doi:10.1364/OE.20.006521 (2012).

54 Park, H. R. *et al.* Resonance behavior of single ultrathin slot antennas on finite dielectric substrates in terahertz regime. *Applied Physics Letters* **96**, 211109, doi:10.1063/1.3437091 (2010).

55 Park, H.-R. *et al.* Terahertz pinch harmonics enabled by single nano rods. *Opt. Express* **19**, 24775-24781, doi:10.1364/OE.19.024775 (2011).

56 Kyoung, J. S., Seo, M. A., Park, H. R., Ahn, K. J. & Kim, D. S. Far field detection of terahertz near field enhancement of sub-wavelength slits using Kirchhoff integral formalism. *Optics Communications* **283**,

4907-4910, doi:http://dx.doi.org/10.1016/j.optcom.2010.08.008 (2010).

57 Robel, I., Bunker, B. A., Kamat, P. V. & Kuno, M. Exciton Recombination Dynamics in CdSe Nanowires: Bimolecular to Three-Carrier Auger Kinetics. *Nano Letters* **6**, 1344-1349, doi:10.1021/nl060199z (2006).

58 Beard, M. C., Turner, G. M. & Schmuttenmaer, C. A. Transient photoconductivity in GaAs as measured by time-resolved terahertz spectroscopy. *Physical Review B* **62**, 15764-15777 (2000).

59 Ralph, S. E., Chen, Y., Woodall, J. & McInturff, D. Subpicosecond photoconductivity of ${\mathrm{In}}_{0.53}${\mathrm{Ga}}_{0.47}$As: Intervalley scattering rates observed via THz spectroscopy. *Physical Review B* **54**, 5568-5573 (1996).

60 Othonos, A., Lioudakis, E., Philipose, U. & Ruda, H. E. Ultrafast carrier dynamics in band edge and broad deep defect emission ZnSe nanowires. *Applied Physics Letters* **91**, 241113, doi:10.1063/1.2825290 (2007).

61 Nolte, D. D. Surface recombination, free-carrier saturation, and dangling bonds in InP and GaAs. *Solid-State Electronics* **33**, 295-298, doi:http://dx.doi.org/10.1016/0038-1101(90)90169-F (1990).

62 Rosenwaks, Y., Shapira, Y. & Huppert, D. Picosecond time-resolved luminescence studies of surface and bulk recombination processes in InP. *Physical Review B* **45**, 9108-9119 (1992).

63 Lloyd-Hughes, J. *et al.* Influence of surface passivation on ultrafast carrier dynamics and terahertz radiation generation in GaAs. *Applied Physics Letters* **89**, 232102, doi:10.1063/1.2398915 (2006).

64 Holzman, J. F. *et al.* Ultrafast carrier dynamics in InP photonic crystals. *Nanotechnology* **16**, 949 (2005).

65 Yablonovitch, E., Sandroff, C. J., Bhat, R. & Gmitter, T. Nearly ideal

electronic properties of sulfide coated GaAs surfaces. *Applied Physics Letters* **51**, 439-441, doi:10.1063/1.98415 (1987).

66 Han, S., Bahk, Y.-M., Park, N. & Kim, D.-S. Terahertz field enhancement in asymmetric and tapered nano-gaps. *Opt. Express* **24**, 2065-2071, doi:10.1364/OE.24.002065 (2016).

67 George, P. A. *et al.* Ultrafast Optical-Pump Terahertz-Probe Spectroscopy of the Carrier Relaxation and Recombination Dynamics in Epitaxial Graphene. *Nano Letters* **8**, 4248-4251, doi:10.1021/nl8019399 (2008).

68 Cunningham, P. D. & Hayden, L. M. Carrier Dynamics Resulting from Above and Below Gap Excitation of P3HT and P3HT/PCBM Investigated by Optical-Pump Terahertz-Probe Spectroscopy. *The Journal of Physical Chemistry C* **112**, 7928-7935, doi:10.1021/jp711827g (2008).

69 Bera, A. & Basak, D. Role of defects in the anomalous photoconductivity in ZnO nanowires. *Applied Physics Letters* **94**, 163119, doi:10.1063/1.3123167 (2009).

70 Sabbah, A. J. & Riffe, D. M. Femtosecond pump-probe reflectivity study of silicon carrier dynamics. *Physical Review B* **66**, 165217 (2002).

71 Guo, W., Zhang, M., Bhattacharya, P. & Heo, J. Auger Recombination in III-Nitride Nanowires and Its Effect on Nanowire Light-Emitting Diode Characteristics. *Nano Letters* **11**, 1434-1438, doi:10.1021/nl103649d (2011).

72 Kerr, M. J. & Cuevas, A. General parameterization of Auger recombination in crystalline silicon. *Journal of Applied Physics* **91**, 2473-2480, doi:10.1063/1.1432476 (2002).

73 Wang, F., Dukovic, G., Knoesel, E., Brus, L. E. & Heinz, T. F. Observation of rapid Auger recombination in optically excited semiconducting carbon nanotubes. *Physical Review B* **70**, 241403

(2004).

74 Robel, I., Gresback, R., Kortshagen, U., Schaller, R. D. & Klimov, V. I. Universal Size-Dependent Trend in Auger Recombination in Direct-Gap and Indirect-Gap Semiconductor Nanocrystals. *Physical Review Letters* **102**, 177404 (2009).

75 Ahn, J. S. *et al.* Optical field enhancement of nanometer-sized gaps at near-infrared frequencies. *Opt. Express* **23**, 4897-4907, doi:10.1364/OE.23.004897 (2015).

76 Ciracì, C. *et al.* Probing the Ultimate Limits of Plasmonic Enhancement. *Science* **337**, 1072-1074, doi:10.1126/science.1224823 (2012).

77 Bennett, B. R., Soref, R. A. & Alamo, J. A. D. Carrier-induced change in refractive index of InP, GaAs and InGaAsP. *IEEE Journal of Quantum Electronics* **26**, 113-122, doi:10.1109/3.44924 (1990).

78 Novotny, L. Effective Wavelength Scaling for Optical Antennas. *Physical Review Letters* **98**, 266802 (2007).

79 Yang, Y. *et al.* Low surface recombination velocity in solution-grown CH3NH3PbBr3 perovskite single crystal. *Nature Communications* **6**, 7961, doi:10.1038/ncomms8961 https://www.nature.com/articles/ncomms8961#supplementary-information (2015).

국문초록

테라파 나노스코피를 통한 반도체 표면 동역학 측정

최근창
물리천문학부
서울대학교

반도체 표면의 전자 동역학은 표면 결함, 이온 도핑, 그리고 대칭 깨짐 등에 의해 벌크의 전자 동역학에 비해 다른 모습을 보인다. 하지만 표면 동역학을 직접적으로 측정하기 위한 기술적인 어려움으로 인해, 그동안의 실험들은 나노선, 나노필름, 또는 양자샘 같이 부피 대 표면적 비율이 높은 제한된 구조를 가지는 물질에서 가능하였다. 본 논문에서는 테라헤르츠 나노 슬랏 안테나로 이루어진 나노스코피 시스템의 강한 전기장 집속을 이용하여 벌크 반도체의 표면 전자 동역학을 측정하였다. 나노 안테나의 폭을 줄이면서 InP와 GaAs의 전자수명이 테라헤르츠 파로 관측가능한 시간해상도의 한계까지 줄어드는 것을 관측하였고, 나노 안테나를 제거 한 후 원래 반도체의 벌크 전자 동역학으로 돌아오는 것을 확인하였다. 또한, 실험결과와 계산결과를 통해, 반도체 물질들의 표면 재결합 속도와 확산계수를 추출하였고, 이러한 방법이 기존의 결과들과 일관성이 있음을 보였다. 이러한 테라파 나노스코피 시스템은 직접적이고 비파괴적인 방법으로 벌크 반도체의 표면 전자 동역학을

측정하는데 새로운 길을 열어줄 것이다.

주요어 : 나노스코피, 광학 펌프 테라파 프루브, 반도체 표면, 전자 동역학

학번 : 2012-30901